The Galaxy Starburst/Main-sequence Bimodality over Five Decades in Stellar Mass at z ≈ 3–6.5

Rinaldi, Pierluigi; Caputi, Karina; van Mierlo, Sophie; Ashby, Matthew L. N.; Bartosch Caminha, Gabriel; Iani, Edoardo

IMPORTANT NOTE: You are advised to consult the publisher's version (publisher's PDF) if you wish to cite from it. Please check the document version below.

Document Version
Publisher's PDF, also known as Version of record

Publication date:
2022

[Link to publication in University of Groningen/UMCG research database](link)

The Galaxy Starburst/Main-sequence Bimodality over Five Decades in Stellar Mass at $z \approx 3$–6.5

Pierluigi Rinaldi[1] , Karina I. Caputi[1,2] , Sophie E. van Mierlo[1] , Matthew L. N. Ashby[3] , Gabriel B. Caminha[1,4] , and
Edoardo Iani[1]

[1] Kapteyn Astronomical Institute, University of Groningen, P.O. Box 800, 9700AV Groningen, The Netherlands; rinaldi@astro.rug.nl
[2] Cosmic Dawn Center (DAWN), Denmark
[3] Center for Astrophysics | Harvard & Smithsonian, 60 Garden St., Cambridge, MA 02138, USA
[4] Max-Planck-Institut für Astrophysik, Karl-Schwarzschild-Str. 1, D-85748 Garching, Germany

Abstract

We study the relation between stellar mass (M_*) and star formation rate (SFR) for star-forming galaxies over approximately five decades in stellar mass ($5.5 \lesssim \log_{10}(M_*/M_\odot) \lesssim 10.5$) at $z \approx 3$–6.5. This unprecedented coverage has been possible thanks to the joint analysis of blank non-lensed fields (COSMOS/SMUVS) and cluster lensing fields (Hubble Frontier Fields) that allow us to reach very low stellar masses. Previous works have revealed the existence of a clear bimodality in the SFR–M_* plane with a star formation Main Sequence and a starburst cloud at $z \approx 4$–5. Here we show that this bimodality extends to all star-forming galaxies and is valid in the whole redshift range $z \approx 3$–6.5. We find that starbursts constitute at least $\approx 20\%$ of all star-forming galaxies with $M_* \gtrsim 10^9 M_\odot$ at these redshifts and reach a peak of 40% at $z = 4$–5. More importantly, 60%–90% of the total SFR budget at these redshifts is contained in starburst galaxies, indicating that the starburst mode of star formation is dominant at high redshifts. Almost all the low stellar mass starbursts with $\log_{10}(M_*/M_\odot) \lesssim 8.5$ have ages comparable to the typical timescales of a starburst event, suggesting that these galaxies are being caught in the process of formation. Interestingly, galaxy formation models fail to predict the starburst/main-sequence bimodality and starbursts overall, suggesting that the starburst phenomenon may be driven by physical processes occurring at smaller scales than those probed by these models.

Unified Astronomy Thesaurus concepts: Galaxy evolution (594); Galaxy formation (595); Starburst galaxies (1570); High-redshift galaxies (734)

1. Introduction

In recent decades, galaxy surveys have constrained several aspects of galaxy evolution up to very high redshifts (e.g., Le Floc'h et al. 2005; Ellis et al. 2013; Oesch et al. 2014; Bouwens et al. 2015; Stefanon et al. 2019; Bowler et al. 2020; Bhatawdekar & Conselice 2021; Bouwens et al. 2021). Much effort has been devoted to constraining galaxy physical properties, such as stellar masses (M_*) and star formation rates (SFRs). These quantities are fundamental in order to probe the process of gas conversion into stars, i.e., the stellar mass assembly (e.g., Casey et al. 2012; L'Huillier et al. 2012; Bauer et al. 2013; Jackson et al. 2020). The statistical analysis of large galaxy samples revealed a correlation between M_* and SFR for star-forming galaxies (e.g., Brinchmann et al. 2004; Elbaz et al. 2007; Daddi et al. 2007; Noeske et al. 2007), the so-called *galaxy main sequence (MS) of star formation*, and the existence of a passive cloud, composed of galaxies whose instantaneous SFRs are negligible with respect to their average past values. These initial works triggered a vast number of later papers studying galaxy evolution on the SFR–M_* plane (e.g., Peng et al. 2010; Speagle et al. 2014; Salmon et al. 2015; Santini et al. 2017).

The existence of a galaxy star formation MS suggests that similar mechanisms could be responsible for growing low- and high-mass galaxies alike (Noeske et al. 2007). The MS galaxies

grow continuously over a long time period from smooth gas accretion (e.g., Sánchez Almeida et al. 2014). The position of a galaxy on the SFR–M_* plane has been proposed to be strictly correlated with its evolutionary stage (e.g., Tacchella et al. 2016), while the intrinsic scatter of the MS suggests some variety in the star formation histories (SFHs) for galaxies of a given stellar mass (e.g., Matthee & Schaye 2019).

Many studies point out that the normalization of the SFR–M_* relation increases with cosmic time (e.g., Whitaker et al. 2012, 2014; Iyer et al. 2018), especially at $z \approx 0$–3, as the gas accretion rate and therefore SFR were higher in the past. The relation between M_* and SFR is generally parameterized as a power law of the form $\log_{10}(\text{SFR}) = \alpha \log_{10}(M_*) + \beta$, where α is the slope and β is the intercept. Various studies have been carried out to determine the slope of this relation and found it to range between 0.6 and 1.0 (see Speagle et al. 2014 and references therein).

Until recently, only a small fraction of star-forming galaxies were known to be placed significantly above the MS in the SFR–M_* plane, which are the so-called *starburst* (SB) galaxies (e.g., Muxlow et al. 2006; Lee et al. 2017; Orlitova 2020). The SB phenomenon is usually driven by a large amount of interstellar gas (mostly in the form of molecular hydrogen), gathered in the galaxy's core. That amount of gas is capable of sustaining the typical timescales of the SB phenomenon ($\approx 10^7$ yr; Heckman 2001). There is no unique definition of an SB galaxy; rather, certain criteria are adopted to identify these sources. For instance, some authors define SBs as sources that lie $N\sigma$ times above the MS (e.g., 4σ times in Rodighiero et al. 2011). In this work, we define as an SB galaxy all those

sources with specific SFR (sSFR) $> 10^{-7.60}$ yr^{-1}, as proposed by Caputi et al. (2017, 2021).

Although many theories have been proposed to explain the SB phenomenon, the nature and growth mechanisms of these galaxies are still under debate. Several works suggest that a violent and large-scale gravitational instability, entirely driven by the self-gravity of the stars, could lead to the SB phenomenon (e.g., Inoue et al. 2016; Romeo & Fathi 2016; Tadaki et al. 2018). Other works propose that an SB galaxy could consist of many discrete bursts of star formation, probably as a consequence of merging events (e.g., Lamastra et al. 2013; Calabrò et al. 2019). In contrast with the interpretation that an SB galaxy could be a mere evolutionary stage of MS galaxies displaying a high star formation efficiency, several papers proposed that SB galaxies could be a sort of primeval galaxies with an anomalously high total gas mass (e.g., Scoville et al. 2014; Genzel et al. 2015; Scoville et al. 2017). Given their rarity, several works concluded that SB galaxies could have played a minor role in the cosmic SFH (e.g., Rodighiero et al. 2011; Sargent et al. 2012; Lamastra et al. 2013). All these works were solely based on the analysis of relatively massive galaxies with $M_* > 10^{10} M_\odot$.

A few years ago, Caputi et al. (2017) discovered the existence of a significant bimodality for star-forming galaxies in the SFR–M_* plane. This study was based on a sample of prominent Hα emitters at $z \approx 4$–5. The bimodality for star-forming galaxies is most evident in the sSFR distribution, which shows two peaks corresponding to the MS and SB cloud. Independently, Bisigello et al. (2018) analyzed a sample of star-forming galaxies at $z = 0$–3 and concluded that the fraction of SBs becomes increasingly higher with redshift and toward low stellar masses. These works provide a clear hint that the SB population could have been much more important than previously thought and suggest that investigating low stellar mass galaxies is essential to fully unveil the SB relevance in the context of galaxy evolution.

Finding the elusive low stellar mass galaxies can be difficult, though. At low redshifts, faint, low stellar mass galaxies are observable in deep blank fields. For instance, Boogaard et al. (2018) made use of the deepest Multi Unit Spectroscopic Explorer (MUSE) observations of Hubble Ultra Deep Field and the Hubble Deep Field South to analyze galaxies reaching stellar masses down to $10^7 M_\odot$ at $z = 0.1$–0.9. At high redshifts we need to combine deep fields and gravitational lensing effects offered by massive galaxy clusters, which magnifies the brightness of background sources (e.g., Pelló et al. 2005). This phenomenon has been successfully exploited to detect intrinsically faint galaxies over a wide redshift range, taking advantage of the flux magnification. As a result, gravitational lensing is a strong tool for better understanding faint, low-mass star-forming galaxies at high redshifts, which would otherwise be inaccessible with current facilities (e.g., Kikuchihara et al. 2020). The study of gravitationally lensed, low stellar mass galaxies at high redshifts indeed suggests that the incidence of SBs among them could be significantly higher than for higher stellar mass objects (e.g., Karman et al. 2017; Caputi et al. 2021).

Here we present a joint analysis of star-forming galaxies in a cosmological blank field, namely, COSMOS/SMUVS (Ashby et al. 2018), and three lensing cluster fields from the Hubble Frontier Fields (HFF) program (Koekemoer et al. 2016; Lotz et al. 2017), allowing us to conduct an unprecedented study of

the SFR–M_* plane over approximately five decades in stellar mass at $z \approx 3$–6.5. This paper is organized as follows. Section 2 provides a brief overview of the data sets used in this work. In Section 3, we describe the sample selection and the photometry. In Section 4, we briefly describe the spectral energy distribution (SED) analysis performed on the sample. In Section 5, we analyze the properties of the lensed Lyα emitters (LAEs). In Section 6, we analyze the SFR–M_* and sSFR–M_* planes, taking into account the HFF and SMUVS galaxies, at $z \approx 3$–6.5. Finally, in Section 7 we present our conclusions. Throughout this paper, we adopt the ΛCDM concordance cosmological model ($H_0 = 70$ km s^{-1} Mpc^{-1}, $\Omega_M = 0.3$, and $\Omega_\Lambda = 0.7$). All magnitudes and fluxes are total, with magnitudes referring to the AB system (Oke & Gunn 1983). Stellar masses and SFRs refer to a Chabrier initial mass function (IMF; Chabrier 2003).

2. Data Sets

2.1. The Hubble Frontier Fields

The HFF program (Koekemoer et al. 2016; Lotz et al. 2017) consists of multicycle Hubble Space Telescope (HST; Tresch-Fienberg 1986) observations to target six galaxy lensing clusters in parallel with six parallel blank field images ($\approx 6'$ from the cluster core). The HFF target clusters were selected based on their lensing power strength and their low/moderate zodiacal and Galactic background. The principal scientific aim of the HFF program is to investigate the high-redshift universe that can only be observed with deep HST observations, showing us first clues of the early universe that, starting next year, we could observe with the James Webb Space Telescope (JWST; Sabelhaus et al. 2005) in more detail.

In this work we consider data from MACS J0416.1$-$2403 (M0416; R.A. = 04:16:09.89, decl. = $-$24:03:58.0), Abell 2744 (A2744; R.A. = 0:14:18.78, decl. = $-$30:23:09.87), and Abell 370 (A370; R.A. = 02:39:52.9, decl. = $-$01:34:36.5). M0416 is a merging galaxy cluster (Mann & Ebeling 2012) at $z = 0.397$ (Ebeling et al. 2014). The total mass is $\approx 1.2 \times 10^{15} M_\odot$ (Grillo et al. 2015), if we consider a radius of 950 kpc. A2744 is a massive X-ray-luminous merging cluster located at $z = 0.308$ (Abell et al. 1989), with a virial mass of $\approx 1.8 \times 10^{15} M_\odot$ within a radius of 1.3 Mpc. Finally, A370 (Abell 1958) is a galaxy cluster at $z = 0.375$ (Struble & Rood 1999). It is well known since it hosts the first-ever detected gravitational arc (Soucail et al. 1987a, 1987b). Therefore, it is one of the best-studied strong-lensing clusters (Medezinski et al. 2010). Several studies of this system suggest that it has a virial mass $\approx 1 \times 10^{15} M_\odot$ (e.g., Umetsu et al. 2011).

2.1.1. HST Imaging

HST employed 840 orbits (140 orbits for each galaxy cluster) to observe the HFF galaxy clusters, achieving a superb depth of ≈ 28.7–29 mag (5σ). Taking into account the gravitational lensing effects, the effective depths of the HFF observations are significantly better (≈ 30–33 mag over very small volumes). For all the HFF targets, HST obtained images with the Advanced Camera for Surveys (ACS) and Wide Field Camera 3 (WFC3), in a total of seven broadband filters (F435W, F606W, F814W, F105W, F125W, F140W, and F160W). We refer the reader to Koekemoer et al. (2016) and Lotz et al. (2017) for further details about the HST data sets. These bands provide an amazing opportunity to probe the

ultraviolet (UV) part of the rest-frame spectrum of the galaxies analyzed in the present work. We obtained all these public data from the Mikulski Archive for Space Telescope.[5] We refer to the v1.0 data release for each galaxy cluster we analyze in this work. The HST images have an angular resolution of $0\rlap{.}''03$ pixel^{-1} and an FWHM of $0\rlap{.}''20$ in the F160W band, which allows for resolving substructures within some galaxies even at high redshifts.

2.1.2. VLT/MUSE Spectroscopic Data

In this work, we analyze data from MUSE (Bacon et al. 2012), an instrument mounted on the Yepun telescope (UT4) at the Very Large Telescope (VLT). It allows us to observe in two different modes: Wide Field Mode (WFM) and Narrow Field Mode (NFM). In this work, we refer to observations carried out with MUSE WFM. WFM allows for integral field spectroscopy over a field of view of 1 arcmin^2, providing a spectrum for each $0\rlap{.}''2 \times 0\rlap{.}''2$ arcseconds^2 pixel element with a point-spread function (PSF) of $\approx 0\rlap{.}''6$–$0\rlap{.}''8$. Therefore, MUSE offers an incredible opportunity to blindly (i.e., without preselection of targets) look for LAEs at $z \approx 2.8$–6.5 behind galaxy clusters. It allows us to cover a spectral range between 4750 and 9350 Å with a spectral resolution of ≈ 2.4 Å reaching LAEs down to 1×10^{-18} erg s^{-1} cm^{-2} in a 1 arcmin^2 field with only 4 hr of exposure.

We make use of MUSE observations covering the three galaxy clusters analyzed in this work.

M0416 is a well-known galaxy cluster of the HFF program. In this work, we refer to the analysis made by Vanzella et al. (2021). It is based on two pointings: the deep pointing as the MUSE Deep Lensed Field (MDLF) centered in the northeast part of the cluster (17.1 hr integration time, 0100.A-0763(A); PI: Vanzella), and the observation in the southwest (11 hr integration, 094.A-0525(A), PI: Bauer). We refer the reader to Bergamini et al. (2021) for detailed information about the lensing model adopted to analyze this cluster.

A2744 was observed with MUSE between 2014 September and 2015 October as part of the Guaranteed Time Observations (GTO) Program (094.A-0115; PI: Richard). The MUSE pointings cover a 2×2 arcmin^2 mosaic with the purpose of covering the entire multiple-image area. The entire area was split into four quadrants, which have been observed for a total of 3.5, 4, 4, and 5 hr. Additional time (2 hr) was used to observe the center of the galaxy cluster. The entire MUSE mosaic overlaps all seven HFF bands we adopt in this work. For detailed information about data reduction and the adopted lensing model, we refer the reader to Mahler et al. (2018).

A370 was observed with MUSE using a large mosaic covering ≈ 4 arcmin^2. This mosaic (096.A-0710(A); PI: Bauer) is an extension of an initial GTO program (094.A-0115(A); PI: Richard), since it is focused on the central part of the galaxy cluster. The entire area covered by the mosaic is 2×2 arcmin^2, centered on the core of the cluster, which allows us to cover nearly the entire multiple-image area. The mosaic comprises 18 hr of on-source exposure, which have been taken from 2014 November to 2016 September. For information about data reduction and the adopted lensing model, we refer the reader to Richard et al. (2021), which provides an updated version of the redshift catalog obtained by Lagattuta et al. (2019).

2.2. The COSMOS/SMUVS Survey

As a complement, we also consider deep imaging data from the COSMOS field (Scoville et al. 2007). By design, these data allow us to explore a very different region in parameter space, as they cover a much wider area than the HFF but are about 3 mag shallower. Therefore, these blank fields are useful to probe the high-mass end, not probed by the lensed fields.

The Spitzer Matching survey of the Ultra-VISTA ultradeep stripes (SMUVS; Ashby et al. 2018) is an Exploration Science Program that collected infrared imaging with Spitzer's data (Werner et al. 2004) with the Infrared Array Camera (IRAC; Fazio et al. 2004) at 3.6 and 4.5 μm over 0.66 deg^2 of the COSMOS field. The region covered by SMUVS corresponds to the part of the COSMOS field with deepest near-IR data from the UltraVISTA program (McCracken et al. 2012) and optical Subaru data (Taniguchi et al. 2007). The SMUVS data have an average integration time of ≈ 25 hr/pointing and reach 80% completeness at ≈ 25.5 mag, in both the 3.6 and 4.5 μm filters (Deshmukh et al. 2018).

In this work we make use of the SMUVS galaxy catalog obtained by Deshmukh et al. (2018) and updated by S. van Mierlo et al. (2022, in preparation). The SMUVS galaxy catalog contains a total of $\approx 300,000$ Spitzer sources extracted using UltraVISTA HK-band-selected galaxies as priors and includes 28-band photometry from the U band through 4.5 μm. Briefly, Deshmukh et al. (2018) and S. van Mierlo et al. (2022, in preparation) adopted the code LePHARE (Arnouts & Ilbert 2011) to perform the SED fitting. They made use of a series of synthetic templates (with solar and subsolar metallicities) from the Bruzual & Charlot (2003, hereafter BC03) library, adopting a simple stellar population (SSP) and different exponentially declining SFHs with star formation time-scales $\tau = 0.01, 0.1, 0.3, 1.0, 3.0, 5.0, 10.0,$ and 15 Gyr. Each synthetic spectrum is attenuated using the reddening rule proposed by Calzetti et al. (2000), leaving the color excess as a free parameter with values $E(B - V) = 0.0$–1.0 in steps of 0.1. We refer the reader to Deshmukh et al. (2018, see Section 3.1) for more details about how this catalog has been obtained. The version of the SMUVS catalog that we consider here has been updated using the latest UltraVISTA data release (DR4).

In this work we only consider star-forming galaxies in SMUVS between $z = 2.8$ and $z = 6.5$, i.e., passive galaxies and active galactic nuclei (AGNs) are excluded. To remove passive galaxies, which account for $\approx 5\%$ of SMUVS sources between $z = 2.8$ and $z = 6.5$, a combination of SED fitting analysis and color criteria has been adopted. We refer the reader to Deshmukh et al. (2018) for more details. In order to exclude any possible AGN contamination, we cross-match our SMUVS sources with the Spitzer MIPS 24 μm catalog (Sanders et al. 2006), adopting a radius of $2''$. We find that $\approx 1\%$ of the SMUVS sources have a flux $S_\nu(24 \, \mu\mathrm{m}) > 0.2$ mJy, which at high redshifts are likely AGNs (Stern et al. 2005). As a double check, we cross-matched those sources with the X-ray catalog from Civano et al. (2016). We find that most of the sources with $S_\nu(24 \, \mu\mathrm{m}) > 0.2$ mJy are X-ray detected. Therefore, we decide to remove all of them as a precaution. Finally, we exclude $\approx 2\%$ of the total SMUVS galaxies that show significant X-ray detections in Civano et al. (2016) and are therefore likely AGNs.

3. Sample Selection and Photometric Analysis

As our main goal here is to study star formation over five decades in stellar mass at $z \gtrsim 3$, we consider two complementary

---

Table 1
Number of Lyα Emitters at Redshift 2.8–6.5 in the HFF Galaxy Clusters

Galaxy Cluster	Number of Sources
MACS J0416.1–2403	134
Abell 2744	139
Abell 370	83

Note. The number of LAEs ($z = 2.8$–6.5) we studied in each galaxy cluster. All these sources have a good quality flag (QF > 1), i.e., sources have either QF = 2 or QF = 3. QF = 2 refers to a probable redshift with a precision less than $\delta z = 0.001$ given by features less strong but still clearly identifiable. QF = 3 refers to a secure redshift with multiple prominent spectral features or one strong feature (such as Lyα). The total amount of all these sources is 356. These correspond to 240 different lensed galaxies. Among them, there are 176 galaxies with a single image and 64 objects with multiple images.

galaxy samples: one consisting of MUSE spectroscopically confirmed LAEs in the three lensing clusters, which mostly span low stellar masses ($\log_{10}(M_*/M_\odot) \approx 6$–$8.5$) at $z = 2.8$–6.5, and the sample of *all* star-forming SMUVS galaxies at the same redshifts, which mostly have $\log_{10}(M_*/M_\odot) > 8.5$. The properties of the latter have been presented and discussed in Deshmukh et al. (2018). In Section 3.3 we summarize the main details of Deshmukh et al.'s sample selection and analysis, but for the lensed LAEs we present a more complete description of the photometric measurements and property derivation, which we have obtained independently of other authors who analyzed partly overlapping galaxy samples (e.g., Merlin et al. 2016; Santini et al. 2017).

3.1. Selection of Lyα Emitters at z > 2.8 in the HFF

In each of the three HFF lensing clusters that we consider here we have selected LAEs at $z \gtrsim 2.8$ using the available MUSE data and keeping only sources with a robust spectroscopic redshift determination (Table 1). Our final sample (M0416 + A2744 + A370) contains 356 imaged sources in total. These correspond to 240 different lensed galaxies. Among these 240 background sources there are 176 with *single* images and 64 objects that have multiple images. The redshift distribution of the analyzed sample is shown in Figure 1.

3.2. HST Photometry of the HFF Lyα Emitters

We used the software Source Extractor (SExtractor; Bertin & Arnouts 1996) to detect the MUSE-selected LAEs and measure their photometry in the seven available HST broad bands. We ran SExtractor in dual-image mode, using an ultradeep detection image (combining data in multiple filters) as the detection image, and measured fluxes on each band separately. In order to maximize the number of detected LAEs, we chose a *hot*-mode configuration in SExtractor, following the method proposed by Galametz et al. (2013), which is optimized for detecting faint sources with small sizes.

We measured each source photometry adopting circular apertures of 0″4 diameter in SExtractor. This small aperture size is necessary to avoid contamination from close neighbors (in projection) and from intracluster light (ICL). As most of our targets are very compact, this aperture size appears to be optimal. However, after a careful visual inspection, we realized that there are some sources for which an aperture size as large as 0″8 diameter is necessary in order to encompass all
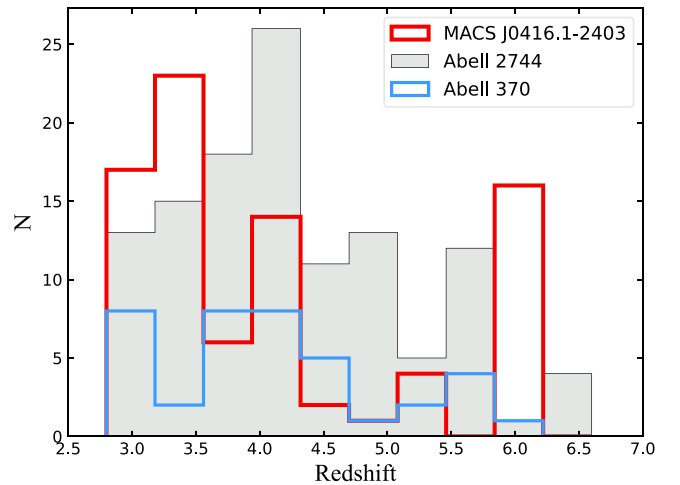
Figure 1. The spectroscopic redshift distribution of analyzed galaxies in each HFF cluster we studied here. Galaxies with multiple lensing images have been considered only once.

the galaxy light (Figure 2). In all cases, we corrected our aperture fluxes to total using the curve of growth of nonsaturated stars in the field. A minority of sources appear significantly stretched by the lensing effects, and for these, circular aperture photometry is clearly not suitable. For these sources, instead, we measured Kron aperture photometry (i.e., MAG_AUTO in SExtractor; Kron 1980). In noncrowded regions of the HST images, we also compared the MAG_APER and MAG_AUTO of each of our targets. If FLUX_AUTO is greater than FLUX_APER corrected with the aperture correction factor, then we kept FLUX_AUTO. Otherwise, we kept FLUX_APER. In this way, we constructed an optimized version of the photometric catalog for each galaxy cluster.

Finally, all our fluxes have been corrected for Galactic extinction.[6] We recover Galactic extinction values that are in perfect agreement with those present in Table 5 of Shipley et al. (2018).

Since SExtractor generally underestimates photometric errors (e.g., Sonnett et al. 2013), we decided to manually set a minimum error of 0.05 mag for all those detections with a photometric error less than that value. Indeed, it represents the minimum systematic error for HST imaging data.

We performed a positional cross-match between our photometric catalogs and the initial MUSE samples. To do that, we adopted a maximum allowed separation of 0″5. In that way, we are able to identify any possible LAE counterpart. The percentages of recovered sources are listed in Table 2. We carefully inspected all the sources that did not yield any HST match to understand why they are not detected by SExtractor. We noticed that, in most cases, they are too faint to be observed even in the ultradeep HST imaging. In other cases, they are close in projection to bright objects (e.g., a bright cluster member), which prevents the individual detection of the faint sources.

In order to perform an independent check of our SExtractor photometry, we compared our photometry with that from ASTRODEEP (Merlin et al. 2016). In particular, we tested our procedure for M0416 and A2744 because they are the only two galaxy clusters that we have in common with

---

[6] We used the tool available at https://irsa.ipac.caltech.edu/applications/DUST/.
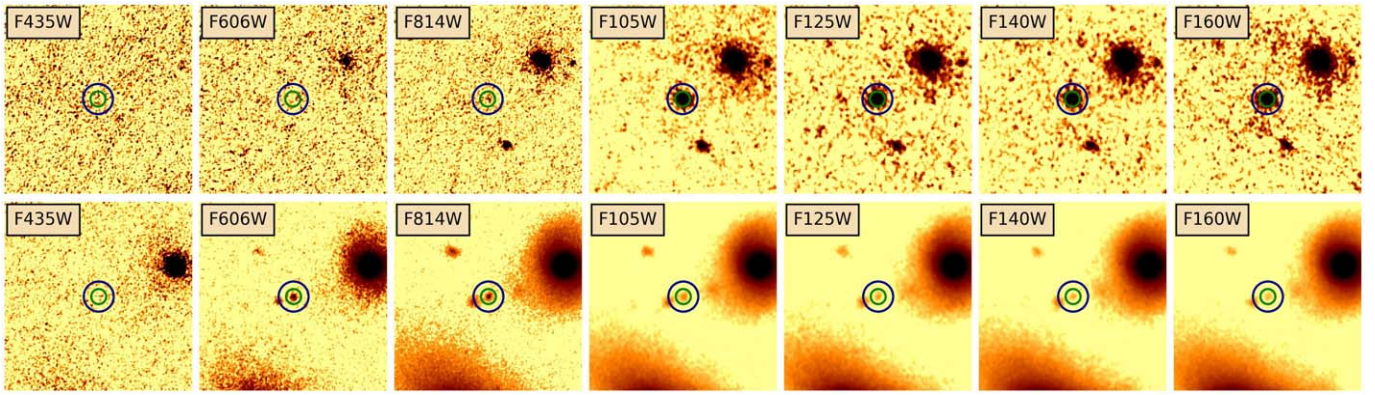
Figure 2. HST postage stamps (5×5 arcsec^2) of two LAEs in A2744. In both cases, we show all the filters considered in this work. In each panel the blue circle indicates an aperture size of $0\rlap{.}''8$ diameter, while the green one refers to an aperture size of $0\rlap{.}''4$ diameter. For the source shown in the top panels an aperture of $0\rlap{.}''8$ is necessary to measure all the galaxy light. On the contrary, for the case at the bottom, an aperture diameter of $0\rlap{.}''4$ is sufficient and prevents light contamination from nearby objects.

Table 2
The Percentages of the Sources Successfully Cross-matched with the Initial MUSE Samples

Galaxy Cluster	Recovered Sources
MACS J0416.1–2403	88%
Abell 2744	81%
Abell 370	84%

Note. These percentages refer to the total amount of sources we found in each galaxy cluster, i.e., both single and multiple images.

them. To do that, we cross-matched our sources with their catalogs, considering an allowed maximum separation of $0\rlap{.}''5$. Despite the different techniques used by the ASTRODEEP group to perform their photometry, our HST photometry is in agreement within the error bars for the vast majority of matched galaxies. We inspected the few galaxies ($\approx 4\%$ in each galaxy cluster we compared) that yielded significant differences in the photometric measurements: in all cases these sources are close in projection to the cluster center. The differences in the measured photometry are therefore not surprising, given that the ASTRODEEP measurements include previous cleaning for ICL. On the one hand, these sources are only $\approx 3\%$ (in the F105W band[7]) of the total sample (M0416 + A2744 + A370). On the other hand, the photometric differences we measured may be due to the different approach used by the ASTRODEEP group. Despite the difference with their photometric measurements, we opted to keep these sources in our study since we do not really know how the ICL cleaning technique could affect the photometry of those sources.

Furthermore, we performed a visual inspection of each source we found in each galaxy cluster to establish the goodness of the cross-matching we carried out with the initial MUSE samples. In that way, we noticed that, in some cases, the centroid of the Lyα emission line falls between two or more sources. Given the size of the MUSE PSF ($\approx 0\rlap{.}''6$–$0\rlap{.}''8$), we are not able to disentangle which of the HST sources is the right counterpart. In these cases, we considered all the objects within a radius of $0\rlap{.}''4$ as counterparts to the LAE. For those sources, we assumed both the same redshift and magnification factor (μ) as for the LAE. Specifically, we found five objects with

multiple ($\geqslant 2$) HST counterparts in M0416, six cases in A2744, and only one case in A370.

3.3. Photometry of the SMUVS Galaxies

The construction of the SMUVS galaxy photometric catalog, which contains fluxes in a total of 28 filters from U through $4.5\,\mu$m, has been thoroughly explained in Deshmukh et al. (2018). Here we only summarize the main information and refer the reader to that paper for further details.

To measure photometry in every band, except the Spitzer bands, SExtractor has been run in dual-image mode, using the UltraVISTA HK_s stack mosaic as the detection image. Here we consider an updated version of the SMUVS catalog, obtained using the latest UltraVISTA release (DR4) as a starting point for the catalog construction (S. van Mierlo et al. 2022, in preparation). The Spitzer IRAC photometry has been obtained using a PSF-fitting technique, using the position of the HK_s sources as priors. This technique is strictly valid only for point-like sources (see Figure 25 of Ashby et al. 2013 for detailed information about how point-like IRAC-detected sources are), but in the Spitzer images this is indeed the case for the vast majority of galaxies at $z > 2$, given the IRAC PSF size (FWHM $\approx 1\rlap{.}''9$; e.g., McCracken et al. 2012; Ashby et al. 2015; Laigle et al. 2016).

All SMUVS photometric measurements have been obtained in circular apertures ($2''$ diameter), corrected to total, and corrected for Galactic extinction.

4. SED Fitting Analysis of the HFF Lyα Emitters

As the SED fitting and redshift derivation of the SMUVS sources have been thoroughly explained by Deshmukh et al. (2018), here we only explain in detail our SED fitting analysis for the HFF LAEs.

Note that while the SED fitting of the SMUVS galaxies is based on 28 filters, we only use seven HST bands from the HFF program to perform the SED fitting of the LAEs. In spite of this difference, the SED fitting quality is still very good in most cases, as for the LAEs the redshifts are securely known in advance from the spectroscopic determinations (Figure 1).

We performed the SED fitting and derived the properties of our LAEs using the code LePHARE. As a starting point, we adopted the same setup as for SMUVS (Deshmukh et al. 2018)

---

[7] We refer to the F105W band because most of the sources are detectable in that filter.

to configure LePHARE. We made use of a galaxy template library with the following set of SFHs:

1. A standard exponentially declining, known as the "τ-model," in which the SFR is SFR(t) ∝ exp $^{-(t-t_0)/\tau}$. In particular, we adopted the following e-folding timescales (τ) in Gyr: 0.01, 0.1, 0.3, 1, 3, 5, 10, 15.
2. An instantaneous burst, adopting an SSP model, which means that a single instantaneous burst of star formation took place at time t: SFR(t) ∝ $\delta(t)$.

We adopted the stellar population synthesis (SPS) models from BC03 based on a Chabrier IMF (Chabrier 2003), considering two different values for the metallicity: solar metallicity ($Z_\odot = 0.02$) and one-fifth of solar metallicity ($Z = 0.2Z_\odot = 0.004$). Since we have high-redshift galaxies (at $z \approx 2.8$–6.5), we chose to expand the range of ages used in Deshmukh et al. (2018) in order to include younger ages as low as 1 Myr. Including these younger ages in our SED fitting analysis prevents an accumulation of results at the youngest allowed age. In order to take into account the effects of internal dust extinction, we convolved the model templates with the Calzetti et al. (2000) reddening law, with the extrapolation proposed by Leitherer et al. (2002) at shorter wavelengths. We considered color excess values between $0 \leqslant E(B-V) \leqslant 1.0$, with a step of 0.1.

In addition, we computed upper limits in every band where SExtractor did not detect any source. We obtained the rms (1σ) of the local background by performing statistics on the flux of 50 empty apertures randomly placed in the background around each source. For LePHARE, we considered a 3σ upper limit for the flux in the corresponding filter and chose the option in which LePHARE ignores any template that produces a flux above that limit. Nevertheless, in a minority of cases (≈3%) the ICL contaminates the light of sources especially in the reddest filters. In these cases, we ignored the photometry in those filters in the SED fitting (we used −99 in LePHARE, which indicates a lack of photometric information).

5. Properties of the HFF Lyα Emitters

5.1. SED-derived Properties

LePHARE returns the best-fit SED and derived parameters for every LAE. As stated above, our total sample contains 356 sources, corresponding to 240 different galaxies. In the following analysis, we will consider only one set of best-fit properties per galaxy, which for the sources with multiple images means that we choose only the best of the best-fit results (i.e., that with the lowest reduced χ^2).

We find that ≈56% of our sample has a subsolar metallicity (0.2 Z$_\odot$) and ≈44% has a solar one (Z$_\odot$). We do not find any correlation between the best-fit metallicity and other parameters considered in our analysis. We find that the best-fit color excess values range from 0.0 to 0.5. In particular, ≈68% of our sources have $E(B-V) = 0.0$ (Figure 3). We find that our values of $E(B-V)$ are in agreement with what has been measured in other populations of LAEs (e.g., Karman et al. 2017; Rosani et al. 2020).

LePHARE also determines the best-fit stellar mass for each galaxy. We correct these values for lensing magnification using the lens model of Bergamini et al. (2021) for M0416, Mahler et al. (2018) for A2744, and Richard et al. (2021) for A370. The magnification factors cover a wide range, with the highest
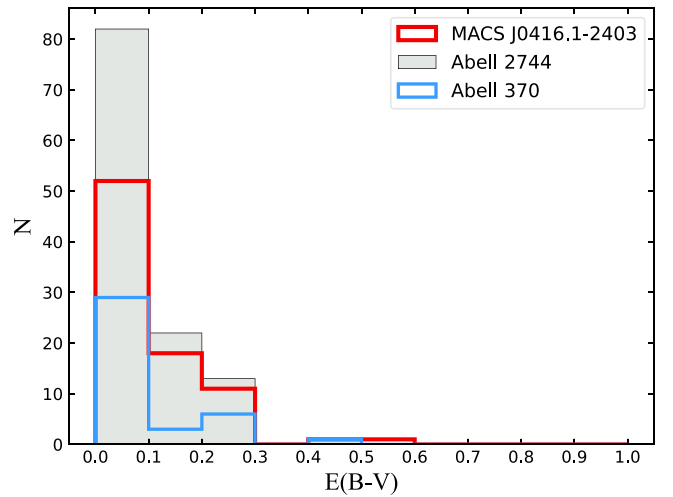

Figure 3. Distribution of color excess obtained through the SED fitting.
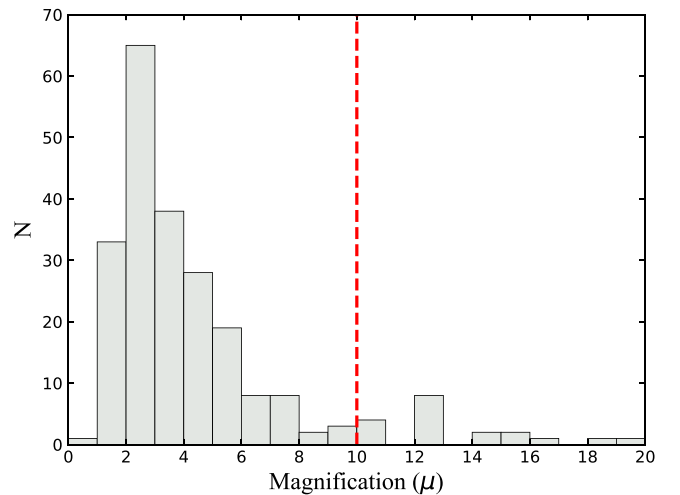

Figure 4. The distribution of the magnification factors for all the HFF galaxy clusters we studied in this work. The red vertical line refers to a limit above which we inspected all the galaxies with $\mu > 10$ in order to analyze whether their presence could have an impact on the SFR−M_* plane or not. To better visualize the distribution, we only show μ up to 20. There are 33 sources with $\mu > 10$ (≈14% of the analyzed sample).

value > 200. The bulk of the sources have a magnification factor < 20. The distribution of magnification values is shown in Figure 4.

The magnification-corrected stellar masses we derived for our galaxies are very low, in the range of $10^{5.5} M_\odot \lesssim M_* \lesssim 10^{10.5} M_\odot$. This range of values is in good agreement with what has been found in the literature in other analyses of (smaller) lensed galaxy samples (e.g., Karman et al. 2017; Meštrić et al. 2022). We show M_* as a function of redshift for our sources in Figure 5. From this figure we see that the complete range of stellar masses is displayed by galaxies at $z < 4.5$, while we only see galaxies with $M_* \lesssim 10^{8.5} M_\odot$ at higher redshifts. This is not surprising because higher stellar mass galaxies become increasingly rarer at higher redshifts and, therefore, larger-area surveys are needed to find them.

These low-mass objects represent a galaxy population almost completely unexplored at these redshifts, with stellar masses even lower than those of the galaxies described in Santini et al. (2017; $M_{*,min} \approx 10^{7.5} M_\odot$). It might be due to a combination of different causes. For instance, our sources have spectroscopic redshifts, and then our SED fitting solutions are well constrained on that
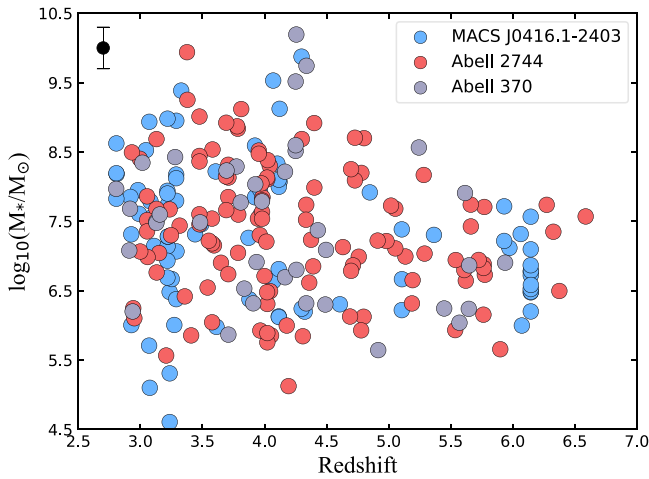
Figure 5. Magnification-corrected stellar masses vs. redshift for our HFF LAEs. Stellar masses are corrected for lensing magnification. The black point in the upper left corner indicates the average stellar mass error.

parameter compared to the Santini et al. (2017) results, which are based on photometric redshifts. We also find that our LAEs have a stellar mass consistent with Karman et al. (2017). However, at the same time, we identify LAEs with unprecedented low stellar masses ($M_* < 10^6 M_\odot$). This result may be due to a combination of the depth of the MUSE data (e.g., the MUSE Deep Lensed Field centered in the northeast part of M0416; Vanzella et al. 2021) and gravitational lensing effects.

These low stellar masses correspond to those of satellite galaxies found in the local universe (e.g., Smith et al. 2019; Wang et al. 2021), and some are even smaller, introducing the possibility that we are looking at stellar aggregates, in the process of forming protogalaxies (e.g., Bromm & Yoshida 2011) or proto−globular clusters (Vanzella et al. 2016, 2017a, 2017b, 2019, 2021). This highlights the advantage of gravitational lensing for investigating intrinsically faint sources, which could otherwise not be observed with current observational facilities in blank fields. Investigating the presence of stellar groups is beyond the scope of this paper; therefore, in the following analysis we will consider that all our lensed objects are galaxies, independently of their derived stellar masses.

5.2. SFR from UV Continuum Emission for the HFF Lyα Emitters

We derived the SFRs for our LAEs independently of their SED fitting by considering their rest-frame UV luminosities (L_ν). To do that, we calculate L_ν at a reference wavelength $\lambda_{\rm rest} = 2000$ Å from the photometry of every galaxy at the filter with closest effective wavelength to $\lambda_{\rm obs} = \lambda_{\rm rest} \times (1 + z)$, where z is the redshift of that galaxy. If the observed wavelength falls in between two passbands, we use the mean flux of those two filters as a proxy for $f(2000$ Å$)$. We correct the UV fluxes for dust extinction following the Calzetti et al. (2000) reddening law in order to recover the intrinsic UV fluxes. To do that, we adopt $E(B − V)$ values from the SED fitting analysis. Then, we convert them into a monochromatic luminosity (L_ν).

Finally, we convert L_ν into an SFR using the prescription given by Kennicutt (1998):

$$\text{SFR } (M_\odot \text{ yr}^{-1}) = 1.4 \times 10^{-28} L_\nu (\text{erg s}^{-1} \text{Hz}^{-1}). \quad (1)$$

Kennicutt's conversion formula (Equation (1)) has a scatter of 0.3 dex. Therefore, we propagate that error into our uncertainty on the SFR and take into account that our SFRs have to be corrected by magnification effects. Furthermore, Kennicutt's formula is based on a Salpeter IMF (Salpeter 1955), while, in this work, we adopt a Chabrier one. We convert our SFRs from a Salpeter IMF to a Chabrier one by multiplication by a factor 0.63 (Madau & Dickinson 2014). The finally obtained SFRs, determined from the observed UV continuum fluxes, range from 0.001 to 158.49 $M_\odot$ yr^{-1}, with a mean of 2.06 $M_\odot$ yr^{-1}.

6. The SFR–M_* and sSFR–M_* Planes

6.1. The Location of the HFF Lyα Emitters

We considered our independent determinations of stellar masses and SFRs to locate our galaxies on the SFR and sSFR versus M_* planes (Figure 6). Multiple studies in the literature have shown that most galaxies, on this plane, appear on the so-called star formation MS (e.g., Brinchmann et al. 2004; Elbaz et al. 2007; Speagle et al. 2014; Whitaker et al. 2014; Salmon et al. 2015), while a minority lie on an SB cloud (e.g., Rodighiero et al. 2011; Caputi et al. 2017; Bisigello et al. 2018). These previous works only studied galaxies down to $\approx 10^{8.5} M_\odot$, while our galaxies probe three decades more down in stellar mass, covering a previously unexplored region in the parameter space.

The location of our lensed LAEs on the SFR−M_* plane shows that more than half ($\approx 52\%$) of these galaxies are located in the SB cloud. This statement must be taken with caution for two reasons. First, until now the SB cloud has only been determined down to $\approx 10^9 M_\odot$ (Caputi et al. 2017) and Figure 6 only shows an extrapolation of the SB lower envelope (Caputi et al. 2021) toward lower stellar masses. Note, however, that this SB lower envelope corresponds to stellar-mass doubling times of only $\approx 4 \times 10^7$ yr, which are the typical timescales for local SB episodes (Knapen & James 2009), and therefore classifying all those objects above that envelope as SBs likely makes sense at any stellar mass.

Second, the reason why we do not see galaxies around the extrapolation of the MS is probably because of selection effects. Although these galaxies could exist, they would not be among the LAEs seen by MUSE in lensing fields. Besides, the mere extrapolation of the known MS would cross the SB envelope at some point at low stellar masses, suggesting that the dichotomy seen at higher stellar masses might not directly apply at lower stellar masses.

We also investigated whether the magnification corrections could be responsible for the very low stellar masses that we derive for some of the LAEs. Fortunately, this is not the case: if we exclude from our sample those sources with $\mu > 10$, which constitute $\approx 14\%$ of the total, we still end up with very low mass objects (down to $\approx 10^{5.5}$–$10^6 M_\odot$).

6.2. The Analysis of the SFR−M_* Plane over Five Decades in Stellar Mass from z = 2.8 to z = 6.5

In order to do a more complete study of the SFR−M_* plane and investigate the evolution of galaxy location with redshift on that plane, we combined our HFF LAE sample with the COSMOS/SMUVS galaxy sample (Deshmukh et al. 2018; S. van Mierlo et al. 2022, in preparation). The latter catalog allows us to incorporate almost 23,000 galaxies at redshifts
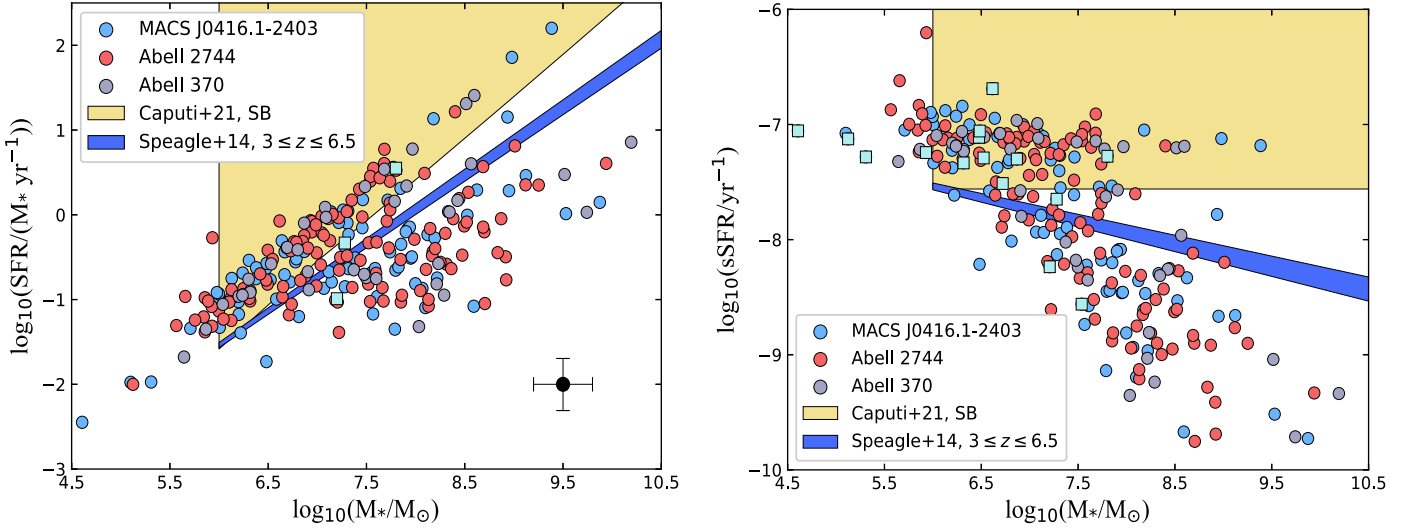
Figure 6. The SFR$-M_*$ plane (left) and the sSFR$-M_*$ plane (right) for our entire sample (M0416 + A2744 + A370) of galaxies at $z = 2.8$–6.5. In both panels, we compare our data points with the lower envelope of SB galaxies adopted in Caputi et al. (2021). We also show the evolution of Speagle's MS prescription (Speagle et al. 2014) as a function of redshift ($z = 3$–6.5). The error bars indicate average uncertainties. The pale blue squares indicate upper limits.
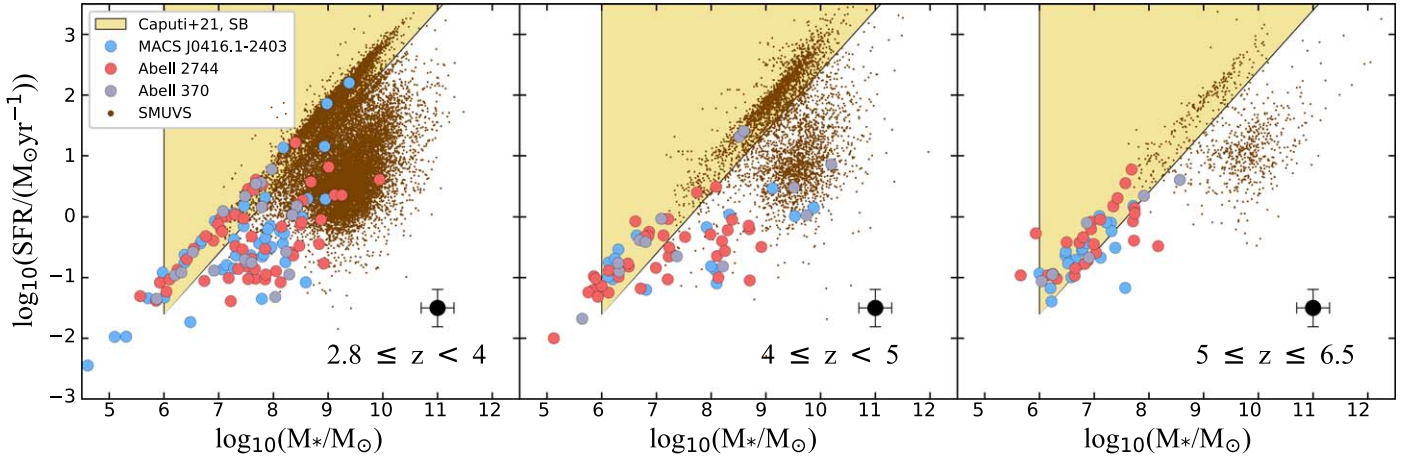
Figure 7. The SFR–M_* plane, populated with all sources (HFF + SMUVS) considered in this work, divided according to redshift interval as indicated. The error bars indicate the average uncertainty estimates. The yellow region indicates for reference the lower envelope of SB galaxies adopted in Caputi et al. (2021).

$z = 2.8$–6.5, which mainly populate the plane at stellar masses $\gtrsim 10^9 \, M_\odot$. These galaxies are only the SMUVS star-forming galaxies with a UV-derived SFR, i.e., passive galaxies from Deshmukh et al. (2018), as well as star-forming galaxies without the necessary photometric information to compute the UV-based SFRs, have been excluded from our analysis. To do that, we applied the same methodology we used for the HFF LAEs.

To analyze the redshift evolution, we split the SFR$-M_*$ plane into three different redshift bins (Figure 7):

1. $2.8 \leqslant z < 4$, with 17,813 objects in total;
2. $4 \leqslant z < 5$, with 4173 sources in total;
3. $5 \leqslant z \leqslant 6.5$, with 866 galaxies in total.

We also analyzed the sSFR distribution taking into account both HFF sources and SMUVS ones (Figure 8).

First of all, we recover the same SB/MS bimodality for star-forming galaxies found by Caputi et al. (2017). This result is not trivial, as Caputi et al. (2017) analyzed only Hα emitters at $z \approx 4$–5 for which the SFRs were based on the inferred

intensities of the Hα line. Our results indicate that the SB/MS bimodality applies to all star-forming galaxies and is independent of the method to infer the SFRs. The region of the SFR$-M_*$ plane between these two sequences is sparsely populated, and it corresponds to a star formation valley (SFV). From Caputi et al. (2017), we divide our entire sample (HFF +SMUVS) into these following three populations:

1. *SB galaxies*: sSFR $> 10^{-7.60} \, \mathrm{yr}^{-1}$;
2. *MS galaxies*: sSFR $< 10^{-8.05} \, \mathrm{yr}^{-1}$;
3. *SFV galaxies*: $10^{-8.05} \, \mathrm{yr}^{-1} \leqslant$ sSFR $\leqslant 10^{-7.60} \, \mathrm{yr}^{-1}$.

We perform a linear regression for the SB and MS galaxies separately in each of our considered redshift bins. We fit the MS and SB sequence adopting the following linear relation:

$$\log_{10}(\mathrm{SFR}/M_\odot \, \mathrm{yr}^{-1}) = \alpha \log_{10}(M_*/M_\odot) + \beta. \quad (2)$$

We obtained the errors on the slopes and intercepts through the bootstrap resampling method. We iterate the bootstrap resampling 1000 times creating a distribution of α and β values and adopt the standard deviation of these distributions as the 1σ
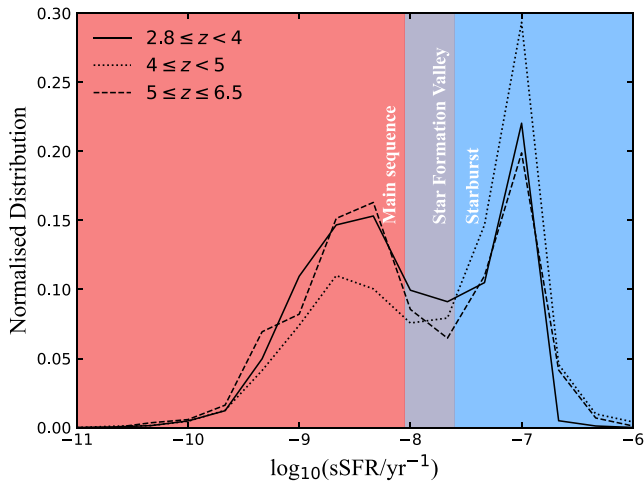
Figure 8. The sSFR distribution of the entire sample (HFF + SMUVS) in each redshift bin. The entire plane is color-coded following the regions derived by Caputi et al. (2017): the star formation MS for sSFR $> 10^{-8.05}$ yr^{-1}, the SB cloud for sSFR $> 10^{-7.60}$ yr^{-1}, and the SFV for $10^{-8.05}$ yr^{-1} $\leqslant$ sSFR $\leqslant$ $10^{-7.60}$ yr^{-1}.

error on those parameters. In particular, to take into account any possible effect of stellar mass completeness that could affect our sample in the different redshift bins that we adopted, we decided to perform the linear regressions considering different stellar-mass cuts.

For the MS galaxies we do not find any significant differences in the slope and intercept values for the different stellar-mass cuts we investigated (i.e., at 10^8, $10^{8.5}$, 10^9, and $10^{9.5}$ $M_\odot$). We applied the same methodology to SB galaxies. However, in this case we considered more stellar-mass cuts than for MS galaxies (i.e., down to $M_{*,\mathrm{min}} = 10^6$ $M_\odot$). Again, we do not find any significant variations even if we go down to very low stellar-mass cuts. To perform the linear regression in the three redshift bins we analyzed in this paper, we decided to consider the following stellar-mass cuts for MS galaxies:

1. $\log_{10}(M_*/M_\odot) \geqslant 9$ at $5 \leqslant z \leqslant 6.5$.
2. $\log_{10}(M_*/M_\odot) \geqslant 8$ at $2.8 \leqslant z < 4$;
3. $\log_{10}(M_*/M_\odot) \geqslant 8.5$ at $4 \leqslant z < 5$.

Regarding SB galaxies, we decided to exploit the unparalleled opportunity offered by the gravitational lensing effect to reach low stellar mass objects, opting for a unique stellar-mass cut at any redshift bins we analyzed in this work (i.e., $\log_{10}(M_*/M_\odot) \geqslant 6$). The results of the linear regressions we performed are listed in Table 3.

In Figure 9 we show our separate MS and SB cloud fittings at $z = 2.8$–4, $z = 4$–5, and $z = 5$–6.5. We find that there is no or very marginal evolution in α for the MS galaxies. Furthermore, we do not see a redshift evolution in the SB sequence. Finally, we recover a large value of β in the MS at $z = 5$–6.5 if compared with the lowest redshift bins. However, we do not observe an evolution within the error bars between $z = 4$–5 and $z = 5$–6.5.

Furthermore, we analyzed whether the presence of the significant peak of sources at $z \approx 6$ in MACS J0416.1–2403 (Figure 5) could affect our results. There are 11 sources in total. We analyzed their M_*, SFRs, and sSFRs. All of them have $M_* < 10^8 M_\odot$. One of them falls in the SFV galaxies ($10^{-8.05}$ yr^{-1} $\leqslant$ sSFR $\leqslant$ $10^{-7.60}$ yr^{-1}). The other ones have sSFR $> 10^{-7.60}$ yr^{-1}. For this reason, we classify all of them
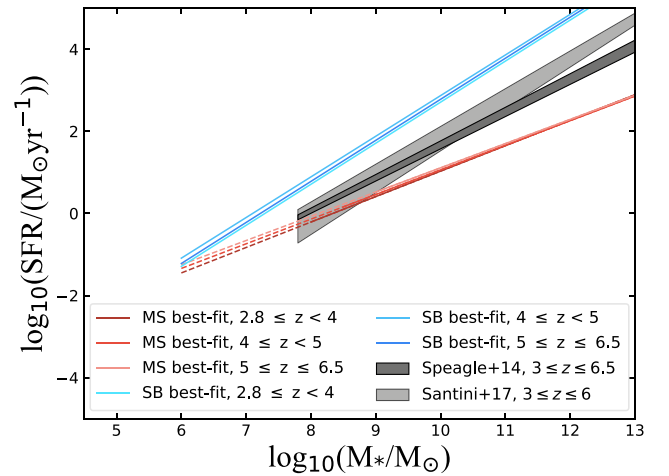

Figure 9. Comparison between our best-fit galaxy MSs and MS determinations from the recent literature: Speagle et al. (2014) and Santini et al. (2017). For them, we show the evolution of the MS in the same redshift interval we analyze in this work. For the MS linear regressions, we adopted three different mass cuts for the three redshift bins we studied: $10^8 M_\odot$ for $2.8 \leqslant z < 4$, $10^{8.5} M_\odot$ for $4 \leqslant z < 5$, and $10^9 M_\odot$ for $5 \leqslant z \leqslant 6.5$. We show their extrapolation down to $10^6 M_\odot$ adopting dashed lines. We also show our SB cloud linear regressions for reference, highlighting that there is no redshift evolution for them within the error bars.

as SB galaxies. Since they are SBs and at $z \approx 6$, we repeated the linear regression for SB galaxies in the third redshift bin ($5 \leqslant z \leqslant 6.5$) without taking them into account. We do not find any significant difference compared to what we show in Table 3. Therefore, we conclude that including them does not affect our results.

To put our results in context, we compared them with the most recent literature about the MS of star-forming galaxies. In Figure 9 we also show the evolution of the MS determinations from Speagle et al. (2014) and Santini et al. (2017) in our same redshift intervals. Note that, as pointed out by Caputi et al. (2017), the comparison must be done with care. Indeed, it could lead to misunderstandings since many authors did not apply the net separation between MS and SB galaxies we adopted in this work (e.g., Rodighiero et al. 2011). As we can see in Figure 9, both Speagle et al. (2014) and Santini et al. (2017) MS prescriptions fall between the MS and SB curves we obtained in this work. This result might be due to the fact that both Speagle et al. (2014) and Santini et al. (2017) do not apply any separation between MS and SB galaxies as we did in this work. Therefore, as we stated above, the comparison of results must be done with care.

6.3. The Role of Starburst Galaxies at z > 3

Over the past decades, the possible existence of different regions on the SFR$-M_*$ plane, as a consequence of different modes of star formation (e.g., Daddi et al. 2010; Genzel et al. 2010; Elbaz et al. 2011), has been studied extensively from the local universe (Renzini & Peng 2015) to $z \approx 3$ (Santini et al. 2009; Rodighiero et al. 2011; Daddi et al. 2013; Ilbert et al. 2015; Bisigello et al. 2018). Daddi et al. (2010) suggested that star formation occurs through two different regimes: a long-lasting mode for disks and a more rapid mode for SBs. There is a broad consensus that MS galaxies grow up on a long timescale as a consequence of a smooth gas accretion from the intergalactic medium (e.g., Sánchez Almeida et al. 2014; Renzini & Peng 2015; Pearson et al. 2018). On the contrary,
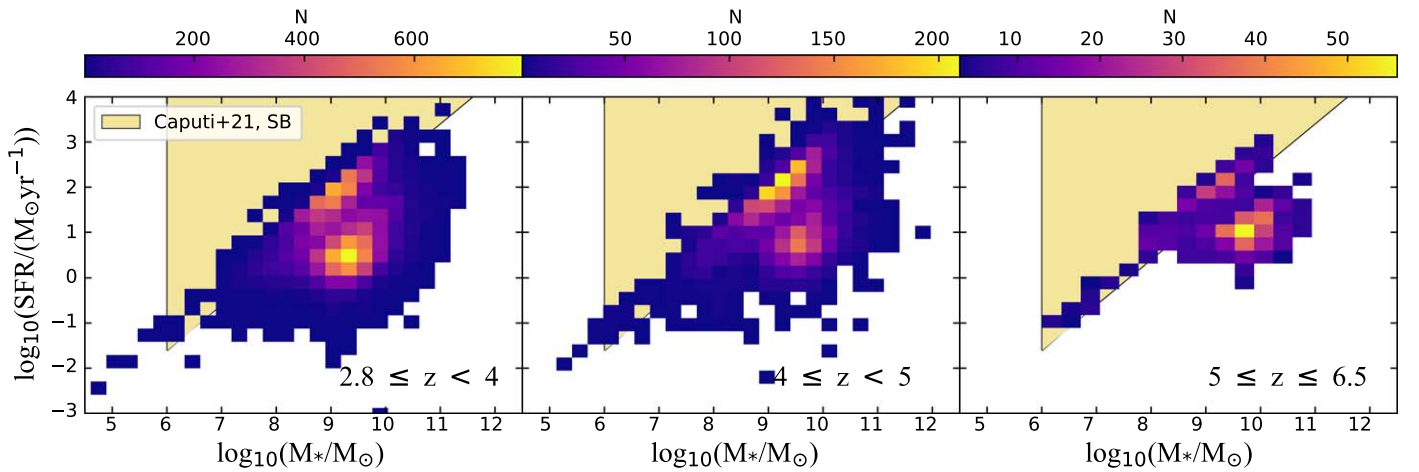
Figure 10. The 2D distributions showing the galaxy distributions (HFF + SMUVS) in the SFR–M_* plane in the three redshift bins adopted in this work, as indicated. The same two prominent features are present in each redshift interval: the SB cloud, and the MS. For reference, the lower envelope of SB galaxies adopted in Caputi et al. (2021) is also shown.

Table 3
Main-sequence and Starburst best-fit Parameters

Redshift	α (MS)	β (MS)	α (SB)	β (SB)
$2.8 \leqslant z < 4$	0.62 ± 0.01	-5.18 ± 0.10	1.00 ± 0.01	-7.29 ± 0.04
$4 \leqslant z < 5$	0.60 ± 0.03	-4.93 ± 0.31	0.99 ± 0.01	-7.03 ± 0.10
$5 \leqslant z \leqslant 6.5$	0.59 ± 0.05	-4.79 ± 0.55	1.00 ± 0.02	-7.22 ± 0.12

Note. The errors on α and β have been estimated adopting the bootstrap resampling method.

the nature of SB galaxies is still under debate, and many theories have been proposed to describe them: violent disk instability (Inoue et al. 2016; Romeo & Fathi 2016; Tadaki et al. 2018), merger events (e.g., Sanders et al. 1988; Elbaz & Cesarsky 2003; Lamastra et al. 2013; Calabrò et al. 2019), and even a sort of primeval galaxies with a high amount of total gas (Scoville et al. 2014; Genzel et al. 2015; Scoville et al. 2017). In particular, the role of SB galaxies in the cosmic history of star formation is not completely understood as well (e.g., Sargent et al. 2012). For instance, Rodighiero et al. (2011) pointed out that, between $z = 1.5$ and $z = 2.5$, SB galaxies represent only 2% of their sample, which account for only 10% of the SFR density (SFRD) in that redshift interval. However, their conclusion is based on massive galaxies only ($M_* > 10^{10} M_\odot$). In this work, instead, we cover a much wider range in stellar mass and show evidence of a prominent SB sequence along with the MS on the SFR$-M_*$ plane in three different redshift bins, from $z \approx 2.8$ to $z \approx 6.5$ (Figure 7), consistent with the findings by Caputi et al. (2017) at $z \approx 4$–5.

In Figure 10, we show the 2D distributions of the SFR$-M_*$ plane as a function of redshift, considering the three redshift bins that we adopted in this work. Our aim with this plot is to quantify the fraction of galaxies in the MS and the SB cloud at each redshift. These 2D distributions clearly show that the SB/MS bimodality discussed above is present at all our analyzed redshifts.

Moreover, we analyzed the fractions of MS, SB, and SFV galaxies, as well as their contribution to the total SFR budget, in each of the redshift bins we adopted in this work. A detailed compilation of the number of galaxies for each population

(MS, SB, and SFV), at different stellar masses and redshifts, is shown in Table 4.
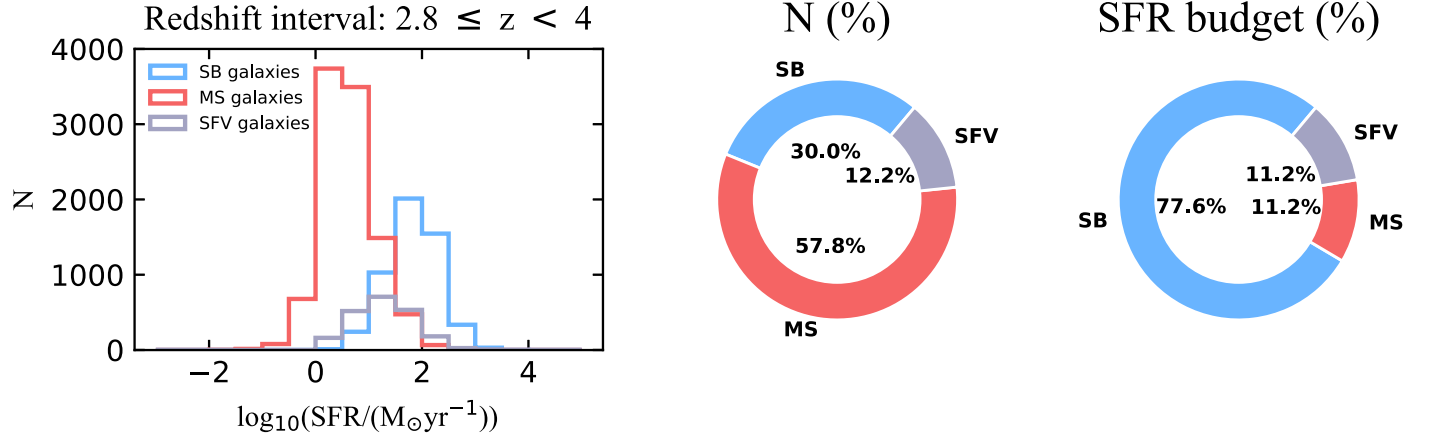
In Figure 11, we show the fraction of MS, SB, and SFV galaxies at $z = 2.8$–4 considering only galaxies with $\log_{10}(M_*/M_\odot) \geqslant 8$, where all three populations are stellar-mass complete at $>70\%$–80% level. We find a high fraction of SB galaxies (30%), much larger than what has been found in the previous literature from the local universe to high redshifts (e.g., Rodighiero et al. 2011; Bergvall et al. 2016; Schreiber et al. 2015; Caputi et al. 2017). The large fraction of SB galaxies we find here is dominated by the low stellar mass galaxies. Remarkably, these SBs constitute $\approx 80\%$ of the total SFR budget at these redshifts, indicating the importance of the SB star formation mode.

We also investigated the evolution of the SB fraction as a function of redshift. To do that, we adopted the same stellar-mass cut ($\log_{10}(M_*/M_\odot) \geqslant 9$) for all redshift bins, in order to ensure high stellar-mass completeness even at the highest redshifts. In Figure 12, we show the fractions of MS, SB, and SFV galaxies with $\log_{10}(M_*/M_\odot) \geqslant 9$ in the three redshift bins, i.e., $z = 2.8$–4, $z = 4$–5, and $z = 5$–6.5.

On the one hand, we find a significantly higher fraction of SB galaxies at $z = 4$–5 than at other redshifts, suggesting the existence of a preferential epoch for the SB phenomenon. On the other hand, we notice a dramatic drop of this fraction at $z > 5$ among the $\log_{10}(M_*/M_\odot) \geqslant 9$ star-forming galaxies. This highlights again that the SB phenomenon preferentially occurs at low stellar masses ($M_* \lesssim 10^9 M_\odot$).

Furthermore, we evaluated whether including sources selected as passive galaxies in the SMUVS sample (see Section 2.2) could really affect our conclusions. To investigate
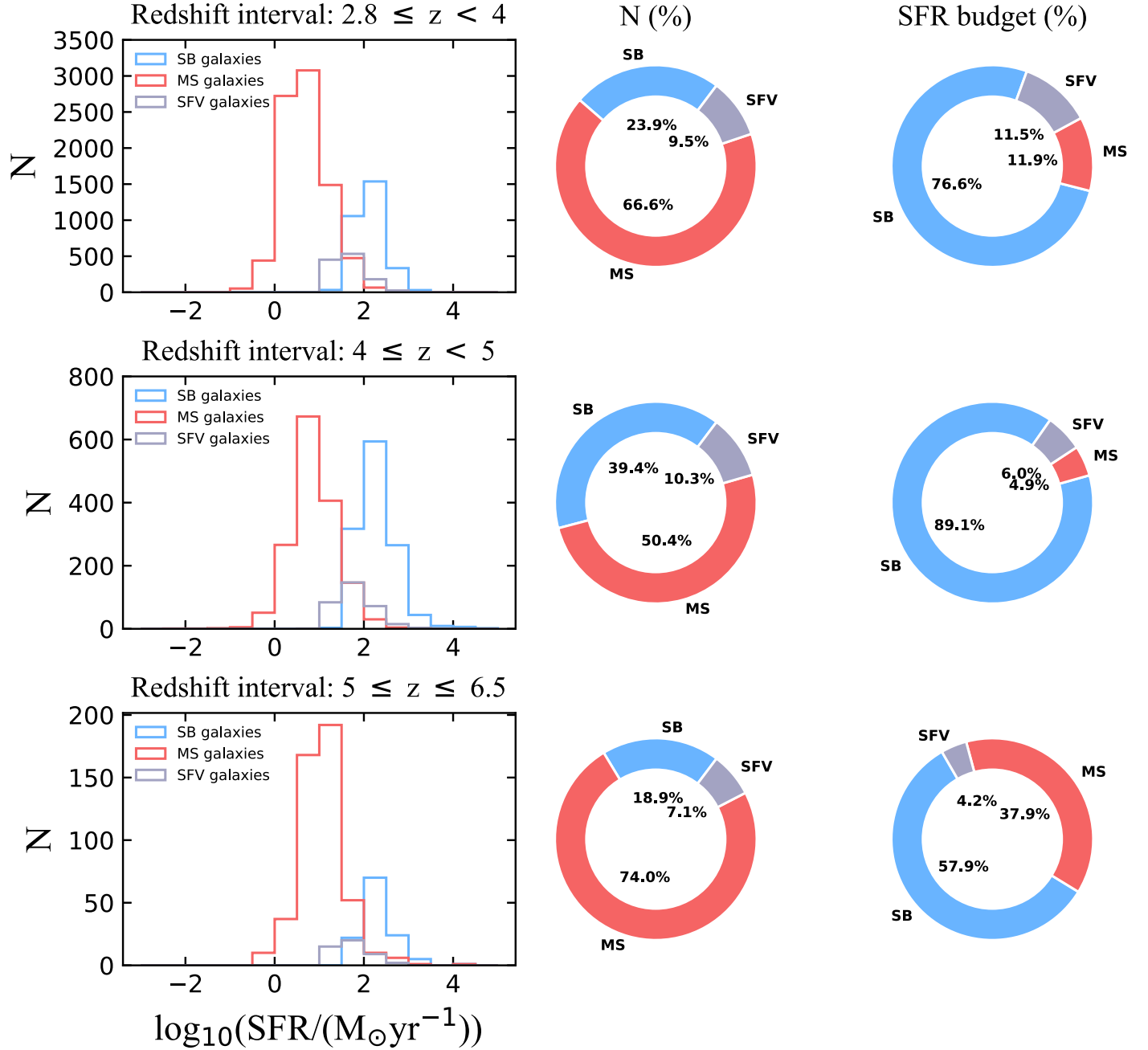
Figure 11. Left panel: SFR distribution of MS, SB, and SFV galaxies at $z = 2.8$–4. Middle panel: a pie chart showing the fraction of MS, SB, and SFV galaxies at $z = 2.8$–4. Right panel: a pie chart showing the percentages contributed to the overall SFR budget by these three galaxy populations. In these plots, we adopted the same stellar-mass cut for MS, SB, and SFV galaxies at $M_* \geqslant 10^8 M_\odot$.

Table 4
Number of Sources (HFF + SMUVS) for Each Population, i.e., MS, SB, and SFV, in the SFR$-M_*$ Plane

Redshift Bin	M_* ($\log_{10}(M_*/M_\odot)$)	MS	SB	SFV	MS Fraction (%)	SB Fraction (%)	SFV Fraction (%)
$2.8 \leqslant z < 4$	$4.5 \leqslant M_* < 5.5$	0	3	0	⋯	⋯	⋯
	$5.5 \leqslant M_* < 6.5$	1	16	0	⋯	⋯	⋯
	$6.5 \leqslant M_* < 7.5$	6	84	12	⋯	⋯	⋯
	$7.5 \leqslant M_* < 8.5$	252	723	425	18.00	51.64	30.36
	$8.5 \leqslant M_* < 9.5$	5735	3764	1348	52.87	34.70	12.43
	$9.5 \leqslant M_* < 10.5$	3897	894	453	74.31	17.05	8.64
	$10.5 \leqslant M_* < 11.5$	190	4	6	95.00	2.00	3.00
	$M_* \geqslant 11.5$	0	0	0	0.00	0.00	0.00
	Total	10,081	5488	2244	56.59	30.81	12.60
$4 \leqslant z < 5$	$4.5 \leqslant M_* < 5.5$	0	1	0	⋯	⋯	⋯
	$5.5 \leqslant M_* < 6.5$	0	19	0	⋯	⋯	⋯
	$6.5 \leqslant M_* < 7.5$	2	33	12	⋯	⋯	⋯
	$7.5 \leqslant M_* < 8.5$	33	241	64	⋯	⋯	⋯
	$8.5 \leqslant M_* < 9.5$	554	1148	252	28.35	58.75	12.90
	$9.5 \leqslant M_* < 10.5$	1033	512	158	60.66	30.06	9.28
	$10.5 \leqslant M_* < 11.5$	85	10	8	82.52	9.71	7.77
	$M_* \geqslant 11.5$	2	0	1	66.67	0.00	33.33
	Total	1715	1964	494	41.10	47.06	11.84
$5 \leqslant z \leqslant 6.5$	$4.5 \leqslant M_* < 5.5$	0	0	0	⋯	⋯	⋯
	$5.5 \leqslant M_* < 6.5$	0	12	1	⋯	⋯	⋯
	$6.5 \leqslant M_* < 7.5$	0	22	6	⋯	⋯	⋯
	$7.5 \leqslant M_* < 8.5$	4	73	8	⋯	⋯	⋯
	$8.5 \leqslant M_* < 9.5$	95	133	47	34.55	48.36	17.09
	$9.5 \leqslant M_* < 10.5$	339	49	20	83.09	12.01	4.90
	$10.5 \leqslant M_* < 11.5$	50	1	1	96.16	1.92	1.92
	$M_* \geqslant 11.5$	6	0	0	100.00	0.00	0.00
	Total	493	290	83	56.93	33.49	9.58

Redshift Bin	MS	SB	SFV	MS Fraction (%)	SB Fraction (%)	SFV Fraction (%)
$2.8 \leqslant z \leqslant 6.5$	12,289	7742	2821	53.77	33.87	12.36

Note. The number and fraction of MS, SB, and SFV galaxies have been reported in each redshift bin and stellar mass bin (1 dex). At the bottom of the table, the total number and fraction of MS, SB, and SFV from $z = 2.8$ to $z = 6.5$ have been reported as well. Blank rows refer to the stellar-mass bins that are significantly incomplete.

Figure 12. Left panels: SFR distributions of MS, SB, and SFV galaxies with $M_* \geqslant 10^9 \, M_\odot$, at different redshift bins. Middle panels: pie charts showing the corresponding fractions of MS, SB, and SFV galaxies. Right panels: pie charts showing the percentages that each population contributes to the overall SFR budget.

this point, we considered all SMUVS galaxies (without separating them into star-forming and passive) and all HFF galaxies and simply made a cut in sSFR: sSFR $> 10^{-9.8}$ yr^{-1}, as suggested in Bisigello et al. (2018). Then, we estimated the fraction of MS, SB, and SFV galaxies at $z = 2.8$–4 considering only galaxies with $\log_{10}(M_*/M_\odot) \geqslant 8$, as we did in Figure 11. In this case, we find that MS galaxies account for 58.7% instead of 57.8%. SB galaxies represent 29.2% of the total amount of sources instead of 30%. Finally, SFV galaxies account for 12.1% instead of 12.2%. This result makes clear that excluding passive galaxies does not affect our results at all.

We estimated the uncertainties on the fractions of MS, SB, and SFV galaxies that we show in Figure 12, via Markov Chain Monte Carlo (MCMC) simulations. We created 1000 mock

catalogs from our initial sample (HFF + SMUVS). To do that, we perturb M_* and SFR within their error bars for each run of MCMC simulations. Moreover, for the SMUVS sources, we decide to perturb redshifts as well because SMUVS galaxies have photometric redshifts in contrast to HFF sources. To do that, we analyze the redshift probability distribution (PDZ) of the SMUVS galaxies. In particular, we focus on those sources that show a secondary peak solution (z_{sec}) with a nonzero probability ($P(z_{sec}) = 1 - P(z_{best})$). We construct our MCMC simulations in order to randomly choose between z_{best} and z_{sec} (when a secondary peak solution exists, i.e., $P(z_{sec}) > 0$), adopting their probabilities as a weight. After we create our mock catalogs, we group mock galaxies according to the three redshift bins we analyzed in this work. Once we have our final mock catalogs, we
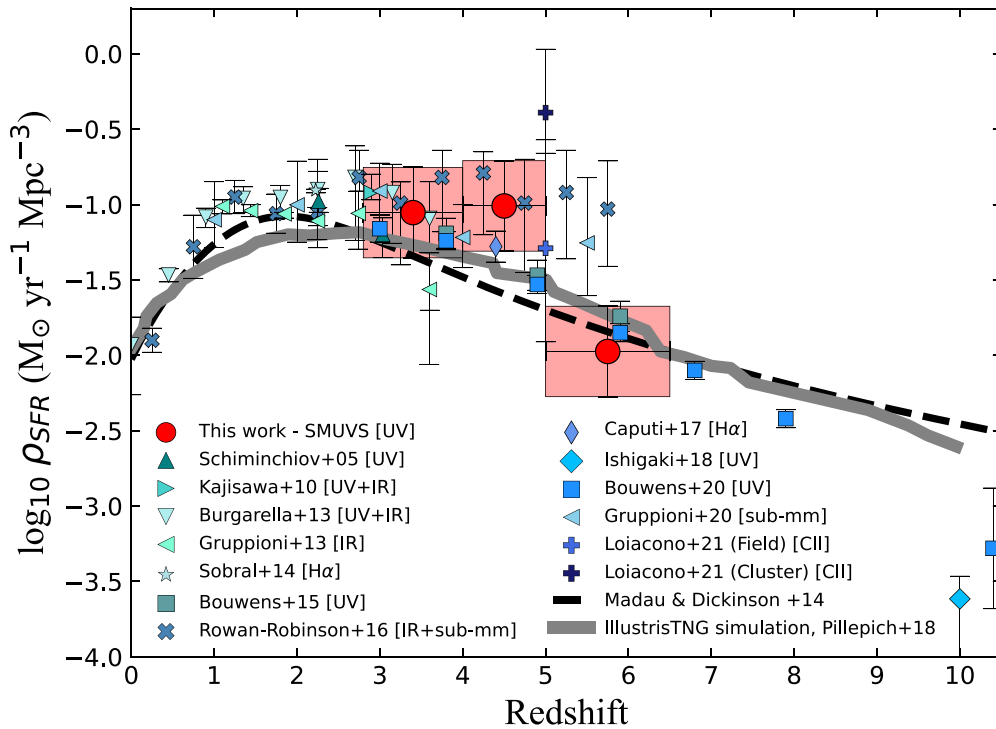
Figure 13. Cosmic SFRD vs. redshift. The large red circles indicate our estimates in the three redshift bins we adopted in this work. To derive those quantities, we estimated the total SFR in each redshift bin, and then we divided that by the corresponding comoving volume. We did not correct our SFRD estimates for incompleteness, which makes them lower limits. All these estimates have been done without taking into account the AGN fraction in the SMUVS catalog at $z \approx 2.8$–6.5. Other symbols refer to the recent SFRD determinations from the literature, based on different SFR tracers (Schiminovich et al. 2005; Kajisawa et al. 2010; Burgarella et al. 2013; Gruppioni et al. 2013; Sobral et al. 2014; Bouwens et al. 2015; Rowan-Robinson et al. 2016; Caputi et al. 2017; Ishigaki et al. 2018; Bouwens et al. 2020; Gruppioni et al. 2020; Loiacono et al. 2021). The different curves correspond to theoretical predictions. Dashed line: Madau & Dickinson (2014). Solid line: Pillepich et al. (2018). All the SFRD values in this figure correspond to a Chabrier (2003) IMF over stellar masses $0.1-100 M_{\odot}$.

split the mock galaxies into MS, SB, and SFV objects, applying the same sSFR criteria explained in Section 6.2. Then, for each mock catalog, we estimate the fraction of MS, SB, and SFV galaxies in all the redshift bins. As a result, for each redshift interval, we construct a distribution of fractions for MS, SB, and SFV galaxies. Finally, we define the 1σ error on those fractions as the half-distance between the 16th and 84th percentile of each distribution. At $z = 2.8$–4 and $z = 4$–5, we recover, for each population, an error of $\approx 1\%$. These errors rise up to $\approx 2\%$ at $z = 5$–6.5.

Another result shown in Figure 12 is that, regardless of the percentage of galaxy types we found in each redshift bin, the majority of the total SFR, even if we apply a stellar-mass cut at $M_* \geqslant 10^9$, is always produced by the SBs. That is particularly true for the second redshift bin since, as shown above, the majority of galaxies at $z = 4$–5 are located in the SB cloud, regardless of the stellar-mass cut we decided to adopt. This result is extremely important because it demonstrates that SB galaxies have had an important role in cosmic SFH, particularly over the first few billion years of cosmic time.

6.4. Implications for the Cosmic Star Formation Rate Density

We use our derived SFRs to obtain an estimate of the cosmic SFRD at $z \approx 2.8$–6.5. To do that, in each redshift interval, we sum SFRs up and then divide them by the comoving volume encompassed by that redshift bin.[8]

In particular, we consider the SMUVS sources only to estimate the SFRD. We decided not to consider the HFF galaxies since they are lensed objects and the computation of the effective volume probed in these fields introduces an additional source of uncertainties from the lens models. Nonetheless, we estimated that the contribution of the HFF galaxies to the total SFR (for HFF + SMUVS) in each redshift bin is negligible ($\lesssim 1\%$).
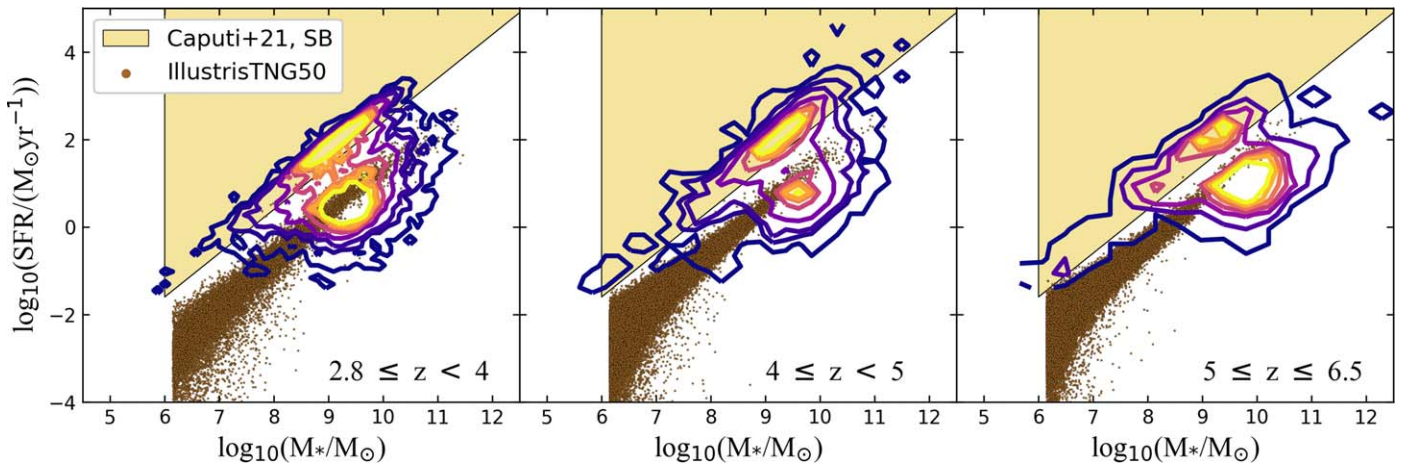
In Figure 13, we show the redshift evolution of the SFRD, the so-called Lilly–Madau diagram (Lilly et al. 1996; Madau et al. 1996). In this plot, we included our derivations of SFRD in the three redshift bin we adopted, as well as a compilation of recent results in the literature that are based on different SFR tracers estimated exploiting different galaxy surveys and individual galaxy SFRs:

1. **UV**: Schiminovich et al. (2005), Bouwens et al. (2015), Ishigaki et al. (2018), and Bouwens et al. (2020).
2. **Emission lines**: Sobral et al. (2014), Caputi et al. (2017), and Loiacono et al. (2021).
3. **IR and submillimeter**: Gruppioni et al. (2013), Rowan-Robinson et al. (2016), and Gruppioni et al. (2020).
4. **Combination of UV and IR**: Kajisawa et al. (2010) and Burgarella et al. (2013).

The SFRD estimates we show in Figure 13 are not corrected for incompleteness, which makes them lower limits.

We find a nearly flat distribution at $z = 2.8$–5. We find a good agreement between our results and those from the recent literature we show, although those results are based on different SFR tracers. Moreover, we find a significant decline of the

---

[8] We estimate the corresponding comoving volume for the SMUVS survey (i.e., 0.66 deg^2). We obtained the comoving volume for the entire sky with the Cosmo calculator at http://www.astro.ucla.edu/~wright/CosmoCalc.html.

Figure 14. The SFR–M_* plane. We show the comparison between observations and simulations. The contour plots refer to our entire sample (HFF + SMUVS). The brown points refer to `IllustrisTNG50` galaxies. We show the SFR–M_* plane in the three redshift bins we adopted. We also show for reference the lower envelope of SB galaxies adopted in Caputi et al. (2021).

SFRD at $z = 5$–6.5, which is probably due to the fact that we miss obscured objects or we are not able to properly recover the correct dust extinction factors, but in agreement with what Bouwens et al. (2015, 2020) found in their work.

Many additional studies have provided SFRD estimations at high redshift in the previous literature (Figure 14). The majority of them, like ours, are based on UV fluxes. However, it is crucial to remember that an estimate based solely on UV fluxes might be heavily influenced by dust extinction corrections, which are higher than those for other SFR tracers. As a result, their estimations are subject to significant uncertainty, particularly at high redshifts (e.g., Castellano et al. 2014).

In spite of these plausible uncertainties, it is clear from Figure 13 that our resulting SFRD value at $z = 4$–5 is significantly higher than most previous determinations from the literature (as compiled by Madau & Dickinson 2014; dashed line) and consistent, within the errors, with far-IR-derived SFRD (e.g., Gruppioni et al. 2013; Rowan-Robinson et al. 2016) and line-emission based SFRD (Caputi et al. 2017; Loiacono et al. 2021). Our inferred SFRD is also significantly above the predictions of the `IllustrisTNG` simulations (gray solid curve; Pillepich et al. 2018). At redshifts up to ≈ 5–5.5, we observe that both the SFRD from the literature and our own derivations have a sharp decline. This is likely the effect of incompleteness—many dust-obscured and/or low-mass galaxies could be missing at such high redshifts.

6.5. The Comparison between Observations and Simulations: IllustrisTNG

We decided to compare our results with the recent IllustrisTNG simulations. The `IllustrisTNG` simulations (Marinacci et al. 2018; Naiman et al. 2018; Nelson et al. 2018; Pillepich et al. 2018; Springel et al. 2018) are cosmological magnetohydrodynamical simulations with the purpose of reproducing processes considered extremely important in the field of galaxy formation and evolution. These simulations are the result of an improvement of the original Illustris project (e.g., Nelson et al. 2015) by including new models such as a new black hole feedback model, magnetohydrodynamics, a new scheme for galactic winds, and many other features. The initial conditions of these simulations have been initialized at

$z = 127$, and the cosmological assumptions are based on Planck Collaboration et al. (2016).

Over the past three years, a number of increasing outcomes have been published to show the agreement between observations and these simulations (e.g., Genel et al. 2018). As a result, `IllustrisTNG` simulations provide an excellent laboratory in which to compare our findings. In this work, we adopted the TNG50 simulation, which is the last simulation of the `IllustrisTNG` project and corresponds to a cosmological box with a side length of 50 Mpc h^{-1} (Nelson et al. 2019). We focused on two important galaxy properties, namely, M_* and SFR, since we want to compare the observed SFR$-M_*$ plane with that derived from the cosmological models.

In Figure 14 we show the SFR$-M_*$ plane where we compare our sample (HFF + SMUVS) with the `IllustrisTNG50` one, in the three redshift bins that we analyzed throughout this work. We can clearly see, in spite of probing a cosmological volume that is significantly larger than the one probed by COSMOS/SMUVS, that `IllustrisTNG50` does not predict the presence of an SB cloud. Instead, `IllustrisTNG50` galaxies lie on a unique tight relation crossing the upper part of our MS.

This lack of SB galaxies can more clearly be seen in the sSFR distribution (Figure 15). Indeed, if we look at the comparison of the sSFR distributions of our sources versus the `IllustrisTNG50` ones, we see that the simulated galaxies do not show any kind of bimodality as we find from the observations. A similar result has been found by Katsianis et al. (2021), although their study is focused on the dichotomy between star-forming and passive galaxies (see also Zhao et al. 2020; Corcho-Caballero et al. 2021). The lack of SB galaxies in theoretical galaxy models was also pointed out for previous generations of galaxy formation models (e.g., Sparre et al. 2015). This SB absence may be due to the insufficient resolution of galaxy models, as the physics involved in the SB phenomenon could occur at very small length scales, which are not properly resolved in state-of-the-art simulations.

7. Discussion and Conclusion

We have investigated the relation between SFR and M_* over five decades in M_*, with a joint analysis of $\approx 23,000$ star-forming galaxies from the COSMOS/SMUVS galaxy survey
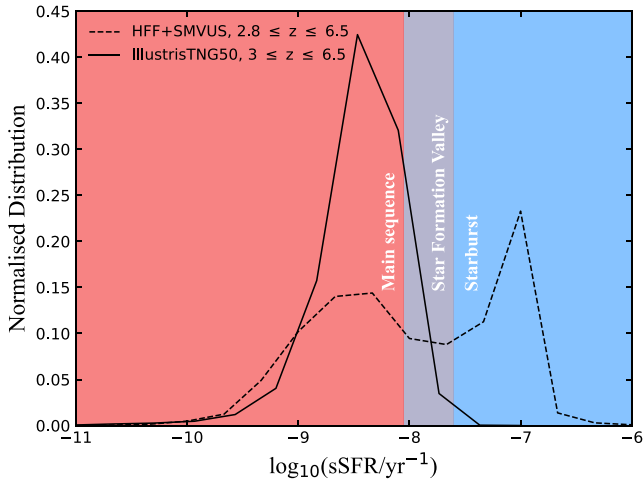
Figure 15. We show the comparison of the sSFR distribution between our entire sample (dashed line) and the IllustrisTNG one (solid line). The entire plane is color-coded following the prescription of Caputi et al. (2017): the MS for sSFR $> 10^{-8.05}$ yr^{-1}, the SB cloud for sSFR $> 10^{-7.60}$ yr^{-1}, and the SFV for $10^{-8.05}$ yr$^{-1} \leqslant$ sSFR $\leqslant 10^{-7.60}$ yr^{-1}.

and a sample of 240 lensed LAEs from three HFF lensing galaxy clusters (M0416, A2744, and A370), all at $2.8 \leqslant z \leqslant 6.5$. We have derived and analyzed their stellar properties. In particular, we considered the rest UV fluxes to estimate the SFR and sSFR for all of these galaxies.

The LAEs that we analyzed here have a stellar mass in the range $10^{5.5} M_\odot \lesssim M_* \lesssim 10^{10.5} M_\odot$, providing an unparalleled chance to study star formation in low stellar mass objects (Figure 6). We still trace stellar masses down to $M_* \approx 10^{5.5}$–$10^6 M_\odot$ even if we only consider galaxies with modest magnification values ($\mu < 10$).

We found that more than half of our LAEs at $z = 3$–6.5 lie on the SB cloud ($\approx 52\%$). This trend is particularly noticeable at low stellar masses. This is likely the consequence of a selection effect: low stellar mass galaxies with lower SFRs may exist, forming the extrapolation of the star formation MS, but are undetected with current telescopes. Interestingly, the ages derived from the best-fit SEDs of our low stellar mass SB are comparable to their stellar-mass doubling times and the SB phenomenon typical timescales ($\approx 10^7$ yr; Heckman 2001), suggesting that we are catching these galaxies in their first SB episode, i.e., in the process of being formed. In the near future, the James Webb Space Telescope will allow us to probe whether older low stellar mass galaxies exist at these high redshifts.

The SMUVS galaxies mainly populate the SFR$-M_*$ plane at stellar masses $\gtrsim 10^9 M_\odot$. in this regime, we found a similar SB/MS bimodality (Figure 8) to that discovered by Caputi et al. (2017). This bimodality recovery is nontrivial: Caputi et al. (2017) only analyzed a sample of Hα emitters at $z \approx 4$–5 and used a different SFR tracer. Our finding is reassuring, as it demonstrates that the presence of SB/MS bimodality does not depend on which SFR tracer is adopted.

We also investigated the evolution of the SFR$-M_*$ plane as a function of redshift at $z = 2.8$–6.5. Following Caputi et al. (2017), we split the SFR$-M_*$ plane into three regions (SB galaxies, MS galaxies, and SFV galaxies). We found basically no evolution in the MS slope, in agreement with previous works. There is no evolution in its normalization either, within the error bars, which instead seems at odds with most of the

previous literature. However, as pointed out by Caputi et al. (2017), the direct comparison of the MS slope and normalization with most previous works could be misleading, as they typically do not segregate SB galaxies in their studies, so their star formation MS appears artificially elevated. For the SB sequence, we also found that it does not evolve at all with redshift within the error bars.

Our results indicate that SBs constitute more than 20% of all star-forming galaxies with $M_* \gtrsim 10^9 M_\odot$ at $2.8 \leqslant z \leqslant 6.5$ and reach a peak of 40% at $z = 4$–5 (Figure 12), suggesting that this redshift range corresponds to a preferential epoch for the SB phenomenon (Faisst et al. 2019; Atek et al. 2022; Vanderhoof et al. 2022). More importantly, although MS galaxies outnumber SB galaxies, we found that, at all redshifts, the majority of the SFR budget is produced by the SB (Figure 12). These results differ from what has been found in most of the previous literature since prior studies only looked at galaxies with $M_* \gtrsim 10^{10} M_\odot$, without taking into account the contribution of low-mass star-forming galaxies. In this work, we also show the implications of these results on the overall cosmic SFRD, strongly suggesting, as we stated above, that SB galaxies played a crucial role in the first few billion years of cosmic time (Figure 13), in agreement with the recent conclusion by Asada et al. (2021).

We have also compared our results with the predictions of the IllustrisTNG50 galaxy simulations. In this work, we show that, at all the redshift intervals that we investigated, simulations cannot reproduce the SB cloud that we identify from observations (Figure 14). Furthermore, galaxy simulations do not predict any SB/MS bimodality. This result is quite clear if we consider the sSFR distribution for observed and simulated galaxies (Figure 15), suggesting a plausible lack of resolution in galaxy models, as the physics involved in the SB phenomenon could occur at very small length scales, which the current hydrodynamical simulations cannot probe. Further observational constraints of the SB stellar and gas contents should help improve this aspect of galaxy models.

Facilities: HST, VLT/MUSE, Spitzer, VISTA, Subaru.

Software: Astropy (Astropy Collaboration et al. 2018), LePHARE (Arnouts & Ilbert 2011), Photutils (Bradley et al. 2021), Source Extractor (Bertin & Arnouts 1996), TOPCAT (Taylor 2005).

ORCID iDs

Pierluigi Rinaldi ⬥ https://orcid.org/0000-0002-5104-8245
Karina I. Caputi ⬥ https://orcid.org/0000-0001-8183-1460
Sophie E. van Mierlo ⬥ https://orcid.org/0000-0001-8289-2863
Matthew L. N. Ashby ⬥ https://orcid.org/0000-0002-3993-0745
Gabriel B. Caminha ⬥ https://orcid.org/0000-0001-6052-3274
Edoardo Iani ⬥ https://orcid.org/0000-0001-8386-3546

References

Abell, G. O. 1958, ApJS, 3, 211
Abell, G. O., Corwin, H. G. J., & Olowin, R. P. 1989, ApJS, 70, 1
Arnouts, S., & Ilbert, O. 2011, LePHARE: Photometric Analysis for Redshift Estimate, Astrophysics Source Code Library, ascl:1108.009
Asada, Y., Ohta, K., & Maeda, F. 2021, ApJ, 915, 47
Ashby, M. L. N., Caputi, K. I., Cowley, W., et al. 2018, ApJS, 237, 39
Ashby, M. L. N., Willner, S. P., Fazio, G. G., et al. 2013, ApJ, 769, 80
Ashby, M. L. N., Willner, S. P., Fazio, G. G., et al. 2015, ApJS, 218, 33
Astropy Collaboration, Price-Whelan, A. M., Sipőcz, B. M., et al. 2018, AJ, 156, 123
Atek, H., Furtak, L., Oesch, P., et al. 2022, MNRAS, 511, 4464
Bacon, R., Accardo, M., Adjali, L., et al. 2012, Msngr, 147, 4
Bauer, A. E., Hopkins, A. M., Gunawardhana, M., et al. 2013, MNRAS, 434, 209
Bergamini, P., Rosati, P., Vanzella, E., et al. 2021, A&A, 645, A140
Bergvall, N., Marquart, T., Way, M. J., et al. 2016, A&A, 587, A72
Bertin, E., & Arnouts, S. 1996, A&AS, 117, 393
Bhatawdekar, R., & Conselice, C. J. 2021, ApJ, 909, 144
Bisigello, L., Caputi, K. I., Grogin, N., & Koekemoer, A. 2018, A&A, 609, A82
Boogaard, L. A., Brinchmann, J., Bouché, N., et al. 2018, A&A, 619, A27
Bouwens, R., González-López, J., Aravena, M., et al. 2020, ApJ, 902, 112
Bouwens, R. J., Illingworth, G. D., Oesch, P. A., et al. 2015, ApJ, 803, 34
Bouwens, R. J., Oesch, P. A., Stefanon, M., et al. 2021, AJ, 162, 47
Bowler, R. A. A., Jarvis, M. J., Dunlop, J. S., et al. 2020, MNRAS, 493, 2059
Bradley, L., Sipőcz, B., Robitaille, T., et al. 2021, astropy/photutils: 1.0.2, 1.0.2, Zenodo, doi:10.5281/zenodo.4453725
Brinchmann, J., Charlot, S., White, S. D. M., et al. 2004, MNRAS, 351, 1151
Bromm, V., & Yoshida, N. 2011, ARA&A, 49, 373
Bruzual, G., & Charlot, S. 2003, MNRAS, 344, 1000
Burgarella, D., Buat, V., Gruppioni, C., et al. 2013, A&A, 554, A70
Calabrò, A., Daddi, E., Fensch, J., et al. 2019, A&A, 632, A98
Calzetti, D., Armus, L., Bohlin, R. C., et al. 2000, ApJ, 533, 682
Caputi, K. I., Caminha, G. B., Fujimoto, S., et al. 2021, ApJ, 908, 146
Caputi, K. I., Deshmukh, S., Ashby, M. L. N., et al. 2017, ApJ, 849, 45
Casey, C. M., Berta, S., Béthermin, M., et al. 2012, ApJ, 761, 140
Castellano, M., Sommariva, V., Fontana, A., et al. 2014, A&A, 566, A19
Chabrier, G. 2003, PASP, 115, 763
Civano, F., Marchesi, S., Comastri, A., et al. 2016, ApJ, 819, 62
Corcho-Caballero, P., Ascasibar, Y., & Scannapieco, C. 2021, MNRAS, 506, 5108
Daddi, E., Dickinson, M., Morrison, G., et al. 2007, ApJ, 670, 156
Daddi, E., Elbaz, D., Walter, F., et al. 2010, ApJL, 714, L118
Daddi, E., Sargent, M. T., Béthermin, M., & Magdis, G. 2013, in IAU Symp. 295, The Intriguing Life of Massive Galaxies, ed. D. Thomas, A. Pasquali, & I. Ferreras (Cambridge: Cambridge Univ. Press), 64
Deshmukh, S., Caputi, K. I., Ashby, M. L. N., et al. 2018, ApJ, 864, 166
Ebeling, H., Ma, C.-J., & Barrett, E. 2014, ApJS, 211, 21
Elbaz, D., & Cesarsky, C. J. 2003, Sci, 300, 270
Elbaz, D., Daddi, E., Le Borgne, D., et al. 2007, A&A, 468, 33
Elbaz, D., Dickinson, M., Hwang, H. S., et al. 2011, A&A, 533, A119
Ellis, R. S., McLure, R. J., Dunlop, J. S., et al. 2013, ApJL, 763, L7
Faisst, A. L., Capak, P. L., Emami, N., Tacchella, S., & Larson, K. L. 2019, ApJ, 884, 133

Fazio, G. G., Hora, J. L., Allen, L. E., et al. 2004, ApJS, 154, 10
Galametz, A., Grazian, A., Fontana, A., et al. 2013, ApJS, 206, 10
Genel, S., Nelson, D., Pillepich, A., et al. 2018, MNRAS, 474, 3976
Genzel, R., Tacconi, L. J., Gracia-Carpio, J., et al. 2010, MNRAS, 407, 2091
Genzel, R., Tacconi, L. J., Lutz, D., et al. 2015, ApJ, 800, 20
Grillo, C., Suyu, S. H., Rosati, P., et al. 2015, ApJ, 800, 38
Gruppioni, C., Béthermin, M., Loiacono, F., et al. 2020, A&A, 643, A8
Gruppioni, C., Pozzi, F., Rodighiero, G., et al. 2013, MNRAS, 436, 2875
Heckman, T. 2001, Encyclopedia of Astronomy and Astrophysics (Murdin) (Boca Raton, FL: CRC Press)
Ilbert, O., Arnouts, S., Le Floc'h, E., et al. 2015, A&A, 579, A2
Inoue, S., Dekel, A., Mandelker, N., et al. 2016, MNRAS, 456, 2052
Ishigaki, M., Kawamata, R., Ouchi, M., et al. 2018, ApJ, 854, 73
Iyer, K., Gawiser, E., Davé, R., et al. 2018, ApJ, 866, 120
Jackson, T. M., Pasquali, A., Pacifici, C., et al. 2020, MNRAS, 497, 4262
Kajisawa, M., Ichikawa, T., Yamada, T., et al. 2010, ApJ, 723, 129
Karman, W., Caputi, K. I., Caminha, G. B., et al. 2017, A&A, 599, A28
Katsianis, A., Xu, H., Yang, X., et al. 2021, MNRAS, 500, 2036
Kennicutt, R. C. J. 1998, ARA&A, 36, 189
Kikuchihara, S., Ouchi, M., Ono, Y., et al. 2020, ApJ, 893, 60
Knapen, J. H., & James, P. A. 2009, ApJ, 698, 1437
Koekemoer, A. M., Mack, J., Lotz, J. M., et al. 2016, AAS Meeting Abstracts, 228, 315.02
Kron, R. G. 1980, ApJS, 43, 305
Lagattuta, D. J., Richard, J., Bauer, F. E., et al. 2019, MNRAS, 485, 3738
Laigle, C., McCracken, H. J., Ilbert, O., et al. 2016, ApJS, 224, 24
Lamastra, A., Menci, N., Fiore, F., & Santini, P. 2013, A&A, 552, A44
Le Floc'h, E., Papovich, C., Dole, H., et al. 2005, ApJ, 632, 169
Lee, N., Sheth, K., Scott, K. S., et al. 2017, MNRAS, 471, 2124
Leitherer, C., Li, I. H., Calzetti, D., & Heckman, T. M. 2002, ApJS, 140, 303
L'Huillier, B., Combes, F., & Semelin, B. 2012, A&A, 544, A68
Lilly, S. J., Le Fevre, O., Hammer, F., & Crampton, D. 1996, ApJL, 460, L1
Loiacono, F., Decarli, R., Gruppioni, C., et al. 2021, A&A, 646, A76
Lotz, J. M., Koekemoer, A., Coe, D., et al. 2017, ApJ, 837, 97
Madau, P., & Dickinson, M. 2014, ARA&A, 52, 415
Madau, P., Ferguson, H. C., Dickinson, M. E., et al. 1996, MNRAS, 283, 1388
Mahler, G., Richard, J., Clément, B., et al. 2018, MNRAS, 473, 663
Mann, A. W., & Ebeling, H. 2012, MNRAS, 420, 2120
Marinacci, F., Vogelsberger, M., Pakmor, R., et al. 2018, MNRAS, 480, 5113
Matthee, J., & Schaye, J. 2019, MNRAS, 484, 915
McCracken, H. J., Milvang-Jensen, B., Dunlop, J., et al. 2012, A&A, 544, A156
Medezinski, E., Broadhurst, T., Umetsu, K., et al. 2010, MNRAS, 405, 257
Merlin, E., Amorín, R., Castellano, M., et al. 2016, A&A, 590, A30
Meštrić, U., Vanzella, E., Zanella, A., et al. 2022, arXiv:2202.09377
Muxlow, T., Beswick, R. J., Richards, A. M. S., & Thrall, H. J. 2006, in Proc. of the 8th European VLBI Network Symp., ed. W. Baan et al. (Trieste: PoS), 31
Naiman, J. P., Pillepich, A., Springel, V., et al. 2018, MNRAS, 477, 1206
Nelson, D., Pillepich, A., Genel, S., et al. 2015, A&C, 13, 12
Nelson, D., Pillepich, A., Springel, V., et al. 2018, MNRAS, 475, 624
Nelson, D., Springel, V., Pillepich, A., et al. 2019, ComAC, 6, 2
Noeske, K. G., Weiner, B. J., Faber, S. M., et al. 2007, ApJL, 660, L43
Oesch, P. A., Bouwens, R. J., Illingworth, G. D., et al. 2014, ApJ, 786, 108
Oke, J. B., & Gunn, J. E. 1983, ApJ, 266, 713
Orlitova, I. 2020, arXiv:2012.12378
Pearson, W. J., Wang, L., Hurley, P. D., et al. 2018, A&A, 615, A146
Pelló, R., Schaerer, D., Richard, J., Le Borgne, J. F., & Kneib, J. P. 2005, in IAU Symp. 225, Gravitational Lensing Impact on Cosmology, ed. Y. Mellier & G. Meylan (Cambridge: Cambridge Univ. Press), 373
Peng, Y.-j., Lilly, S. J., Kovač, K., et al. 2010, ApJ, 721, 193
Pillepich, A., Springel, V., Nelson, D., et al. 2018, MNRAS, 473, 4077
Planck Collaboration, Ade, P. A. R., Aghanim, N., et al. 2016, A&A, 594, A13
Renzini, A., & Peng, Y.-j 2015, ApJL, 801, L29
Richard, J., Claeyssens, A., Lagattuta, D., et al. 2021, A&A, 646, A83
Rodighiero, G., Daddi, E., Baronchelli, I., et al. 2011, ApJL, 739, L40
Romeo, A. B., & Fathi, K. 2016, MNRAS, 460, 2360
Rosani, G., Caminha, G. B., Caputi, K. I., & Deshmukh, S. 2020, A&A, 633, A159
Rowan-Robinson, M., Oliver, S., Wang, L., et al. 2016, MNRAS, 461, 1100
Sabelhaus, P. A., Campbell, D., Clampin, M., et al. 2005, Proc SPIE, 5899, 241
Salmon, B., Papovich, C., Finkelstein, S. L., et al. 2015, ApJ, 799, 183
Salpeter, E. E. 1955, ApJ, 121, 161
Sánchez Almeida, J., Elmegreen, B. G., Muñoz-Tuñón, C., & Elmegreen, D. M. 2014, A&ARv, 22, 71

Sanders, D., Scoville, N., Aussel, H., et al. 2006, S-COSMOS: The MIPS Deep Survey of the COSMOS 2-sqdeg Field, Spitzer Proposal #30143

Sanders, D. B., Soifer, B. T., Elias, J. H., et al. 1988, ApJ, 325, 74

Santini, P., Fontana, A., Castellano, M., et al. 2017, ApJ, 847, 76

Santini, P., Fontana, A., Grazian, A., et al. 2009, A&A, 504, 751

Sargent, M. T., Béthermin, M., Daddi, E., & Elbaz, D. 2012, ApJL, 747, L31

Schiminovich, D., Ilbert, O., Arnouts, S., et al. 2005, ApJL, 619, L47

Schreiber, C., Pannella, M., Elbaz, D., et al. 2015, A&A, 575, A74

Scoville, N., Aussel, H., Brusa, M., et al. 2007, ApJS, 172, 1

Scoville, N., Aussel, H., Sheth, K., et al. 2014, ApJ, 783, 84

Scoville, N., Lee, N., Vanden Bout, P., et al. 2017, ApJ, 837, 150

Shipley, H. V., Lange-Vagle, D., Marchesini, D., et al. 2018, ApJS, 235, 14

Smith, R., Pacifici, C., Pasquali, A., & Calderón-Castillo, P. 2019, ApJ, 876, 145

Sobral, D., Best, P. N., Smail, I., et al. 2014, MNRAS, 437, 3516

Sonnett, S., Meech, K., Jedicke, R., et al. 2013, PASP, 125, 456

Soucail, G., Fort, B., Mellier, Y., & Picat, J. P. 1987a, A&A, 172, L14

Soucail, G., Mellier, Y., Fort, B., Mathez, G., & Cailloux, M. 1987b, Msngr, 50, 5

Sparre, M., Hayward, C. C., Springel, V., et al. 2015, MNRAS, 447, 3548

Speagle, J. S., Steinhardt, C. L., Capak, P. L., & Silverman, J. D. 2014, ApJS, 214, 15

Springel, V., Pakmor, R., Pillepich, A., et al. 2018, MNRAS, 475, 676

Stefanon, M., Labbé, I., Bouwens, R. J., et al. 2019, ApJ, 883, 99

Stern, D., Eisenhardt, P., Gorjian, V., et al. 2005, ApJ, 631, 163

Struble, M. F., & Rood, H. J. 1999, ApJS, 125, 35

Tacchella, S., Dekel, A., Carollo, C. M., et al. 2016, MNRAS, 457, 2790

Tadaki, K., Iono, D., Yun, M. S., et al. 2018, Natur, 560, 613

Taniguchi, Y., Scoville, N., Murayama, T., et al. 2007, ApJS, 172, 9

Taylor, M. B. 2005, in ASP Conf. Ser. 347, Astronomical Data Analysis Software and Systems XIV, ed. P. Shopbell, M. Britton, & R. Ebert (San Francisoc, CA: ASP), 29

Tresch-Fienberg, R. 1986, S&T, 72, 562

Umetsu, K., Broadhurst, T., Zitrin, A., et al. 2011, ApJ, 738, 41

Vanderhoof, B. N., Faisst, A. L., Shen, L., et al. 2022, MNRAS, 511, 1303

Vanzella, E., Calura, F., Meneghetti, M., et al. 2017a, MNRAS, 467, 4304

Vanzella, E., Calura, F., Meneghetti, M., et al. 2019, MNRAS, 483, 3618

Vanzella, E., Caminha, G. B., Rosati, P., et al. 2021, A&A, 646, A57

Vanzella, E., Castellano, M., Meneghetti, M., et al. 2017b, ApJ, 842, 47

Vanzella, E., De Barros, S., Cupani, G., et al. 2016, ApJL, 821, L27

Wang, W., Takada, M., Li, X., et al. 2021, MNRAS, 500, 3776

Werner, M. W., Roellig, T. L., Low, F. J., et al. 2004, ApJS, 154, 1

Whitaker, K. E., Franx, M., Leja, J., et al. 2014, ApJ, 795, 104

Whitaker, K. E., van Dokkum, P. G., Brammer, G., & Franx, M. 2012, ApJL, 754, L29

Zhao, P., Xu, H., Katsianis, A., & Yang, X.-H. 2020, RAA, 20, 195